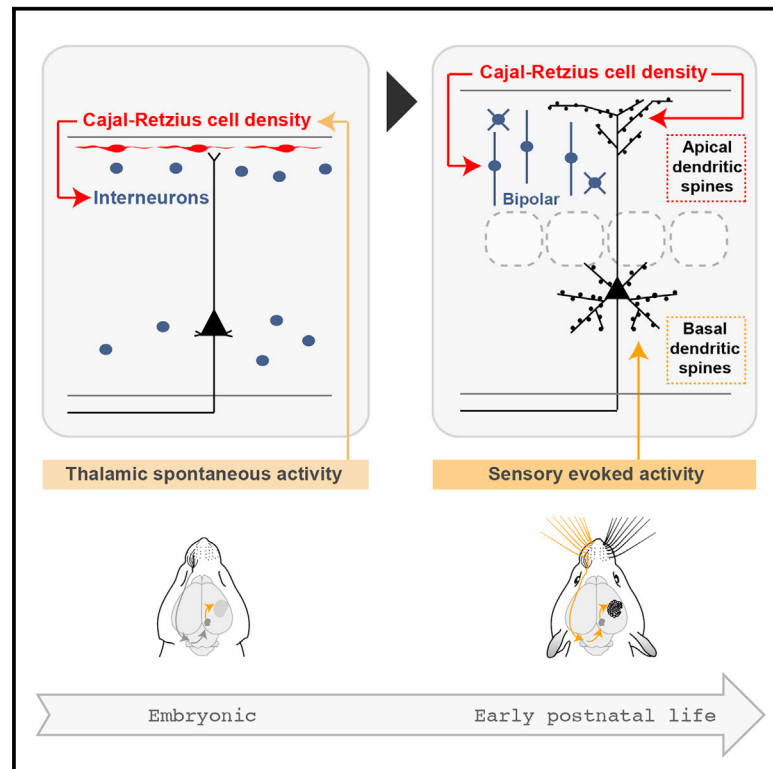# Dynamic interplay between thalamic activity and Cajal-Retzius cells regulates the wiring of cortical layer 1

Graphical abstract

Highlights

- Prenatal thalamic waves of activity regulate CRc density in L1

- Prenatal and postnatal CRc manipulations alter specific interneuron populations

- Postnatal CRc shape L5 apical dendrite structural and functional properties

- Early sensory activity selectively regulates L5 basal dendrite spine formation

Authors

Ioana Genescu, Mar Aníbal-Martínez, Vladimir Kouskoff, ..., Guillermina López-Bendito, Frédéric Gambino, Sonia Garel

Correspondence

sonia.garel@bio.ens.psl.eu

In brief

Genescu et al. show that the wiring of cortical layer 1 relies on crosstalk between spontaneous thalamic activity and Cajal-Retzius cells, with long-lasting consequences on cortical circuits. These findings reveal that transient activity and cells play key roles in the wiring of apical dendrites and upper layer neocortical networks.

CelPress

Cell Reports

Article

Dynamic interplay between thalamic activity and Cajal-Retzius cells regulates the wiring of cortical layer 1

Ioana Genescu,[1] Mar Aníbal-Martínez,[2] Vladimir Kouskoff,[3] Nicolas Chenouard,[3] Caroline Mailhes-Hamon,[4] Hugues Cartonnet,[1] Ludmilla Lokmane,[1] Filippo M. Rijli,[5,6] Guillermina López-Bendito,[2] Frédéric Gambino,[3] and Sonia Garel[1,7,8,*]

[1]Institut de Biologie de l'École Normale Supérieure (IBENS), Département de Biologie, École Normale Supérieure, CNRS, INSERM, Université PSL, 75005 Paris, France
[2]Instituto de Neurociencias de Alicante, Universidad Miguel Hernandez, Sant Joan d'Alacant, Spain
[3]University of Bordeaux, CNRS, Interdisciplinary Institute for Neuroscience, IINS UMR 5297, 33000 Bordeaux, France
[4]Acute Transgenesis Facility, Institut de Biologie de l'École Normale Supérieure (IBENS), École Normale Supérieure, CNRS, INSERM, PSL Université Paris, 75005 Paris, France
[5]Friedrich Miescher Institute for Biomedical Research, 4058 Basel, Switzerland
[6]University of Basel, 4056 Basel, Switzerland
[7]Collège de France, 75005 Paris, France
[8]Lead contact
*Correspondence: sonia.garel@bio.ens.psl.eu
https://doi.org/10.1016/j.celrep.2022.110667

SUMMARY

Cortical wiring relies on guidepost cells and activity-dependent processes that are thought to act sequentially. Here, we show that the construction of layer 1 (L1), a main site of top-down integration, is regulated by crosstalk between transient Cajal-Retzius cells (CRc) and spontaneous activity of the thalamus, a main driver of bottom-up information. While activity was known to regulate CRc migration and elimination, we found that prenatal spontaneous thalamic activity and NMDA receptors selectively control CRc early density, without affecting their demise. CRc density, in turn, regulates the distribution of upper layer interneurons and excitatory synapses, thereby drastically impairing the apical dendrite activity of output pyramidal neurons. In contrast, postnatal sensory-evoked activity had a limited impact on L1 and selectively perturbed basal dendrites synaptogenesis. Collectively, our study highlights a remarkable interplay between thalamic activity and CRc in L1 functional wiring, with major implications for our understanding of cortical development.

INTRODUCTION

The neocortex controls sensory perception, motor control, or cognition via exquisite neuronal networks formed by excitatory pyramidal neurons (principal cells) and GABAergic inhibitory interneurons (Bartolini et al., 2013; Harris and Shepherd, 2015). The construction of cortical circuits relies on both core genetic programs and neuronal activity (Sur and Rubenstein, 2005). In particular, the thalamus, which provides the sensorimotor bottom-up information has been shown to play major roles in the development of cortical circuits. For instance, postnatal thalamic activity regulates the morphology, functional maturation, and integration of both principal cells and cortical interneurons (Callaway and Borrell, 2011; Che et al., 2018; Cossart, 2011; De Marco García et al., 2011, 2015; Jabaudon et al., 2012; Kastli et al., 2020; Li et al., 2013; Modol et al., 2020; Tuncdemir et al., 2015). In addition, prenatal and perinatal spontaneous activity derived from sensory organs or directly from the thalamus has recently been shown to play an earlier role in shaping neocortical

assemblies and network maturation (Ackman et al., 2012; Ackman and Crair, 2014; Antón-Bolaños et al., 2019; Arroyo and Feller, 2016; Babola et al., 2018; Blankenship and Feller, 2010; Hanganu et al., 2002; Martini et al., 2021; Mizuno et al., 2018; Modol et al., 2020; Moreno-Juan et al., 2017). Deciphering the relative contributions of spontaneous versus sensory-evoked thalamic activity is essential for our comprehension of the mechanisms regulating cortical wiring.

The mature architecture of the neocortex enables circuits to integrate bottom-up thalamic sensory information with top-down information that provides context, value, and feedback from internal representations (Harris and Shepherd, 2015; Keller and Mrsic-Flogel, 2018; Schuman et al., 2021). Anatomically, layer 1 (L1), the most superficial layer of the neocortex, has emerged as a major site for top-down modulation (Cauller, 1995; Cruikshank et al., 2012; Ibrahim et al., 2021; Schuman et al., 2021), with axonal inputs targeting apical dendrites of both upper and deep cortical layers (Abs et al., 2018; Cruikshank et al., 2012; Gambino et al., 2014; Hartung and Letzkus, 2021;
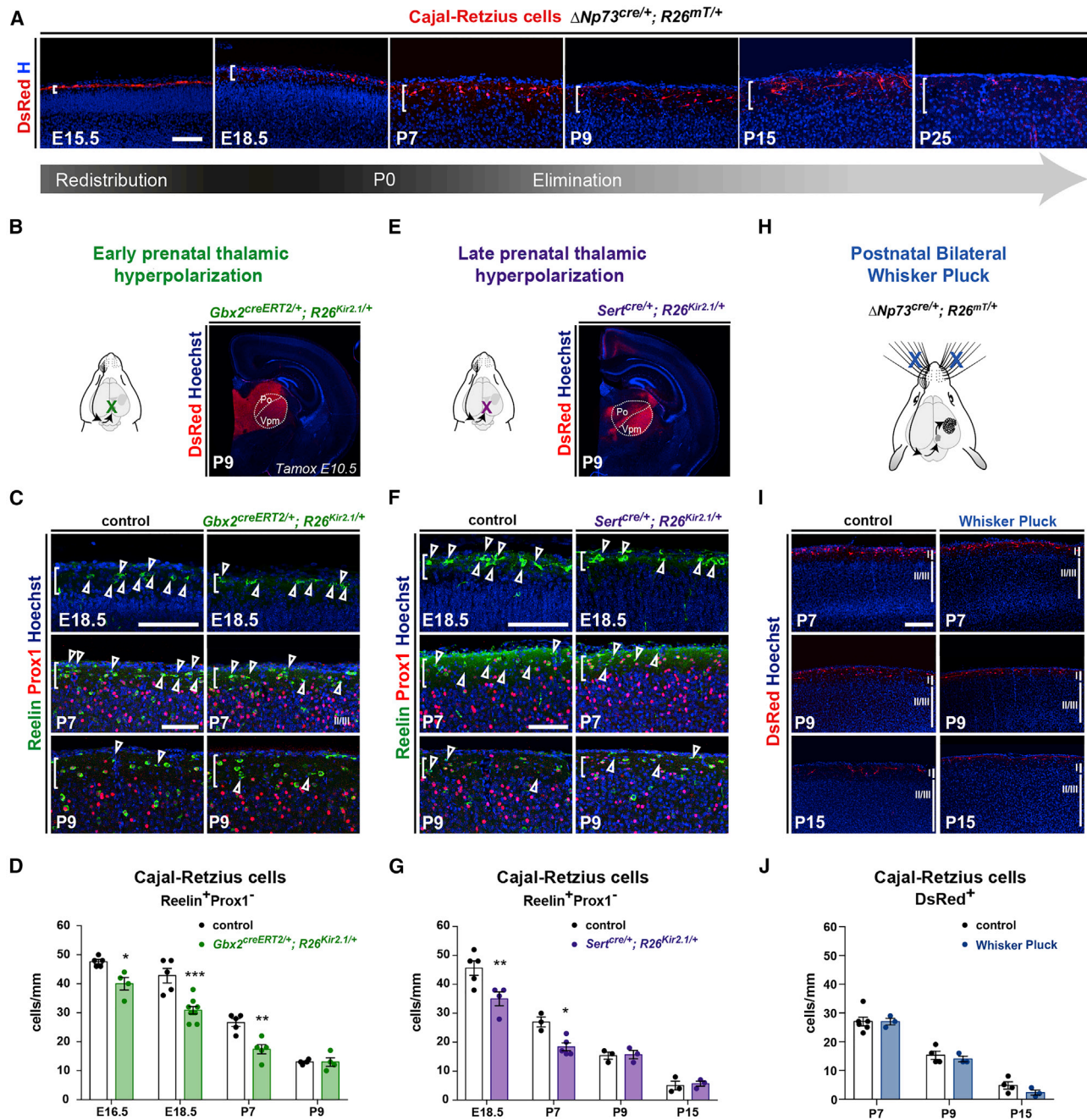
Figure 1. Thalamic activity regulates CRc prenatal distribution but not their postnatal elimination

(A) Confocal images of sections in the somatosensory cortex from E15.5 to P25, illustrating L1 dynamics of CRc labeled with $\Delta Np73^{cre/+};R26^{mT/+}$.

(B) Schematic representation of thalamic hyperpolarization using the $Gbx2^{creERT2/+}$ line (with an E10.5 tamoxifen administration), which drives the expression of the Kir2.1 channel in most thalamic nuclei, as illustrated at P9.

(C) Confocal images of sections in the barrel cortex at E18.5, P7, and P9 of controls and $Gbx2^{creERT2/+};R26^{Kir2.1/+}$ to identify CRc as L1 Reelin^{+} cells embryonically, and Reelin[+]Prox1^{−} cells postnatally (arrowheads).

(D) Quantification of CRc density (cells/mm of L1 length) shows a striking reduction in E16.5, E18.5, and P7 mutants, whereas this difference is not observed any longer at P9 (E16.5: n = 5 controls, n = 4 mutants; E18.5: n = 5 controls, n = 8 mutants; P7: n = 5 controls, n = 5 mutants; and P9: n = 4 controls, n = 4 mutants).

(E) Schematic representation of thalamic hyperpolarization using the $Sert^{cre/+}$ line, which drives the expression of the Kir2.1 channel in the sensory thalamus from the end of embryogenesis, as illustrated at P9.

(F) Confocal images of sections in the barrel cortex at E18.5, P7, and P9 of controls and $Sert^{cre/+};R26^{Kir2.1/+}$ pups to identify CRc as L1 Reelin^{+} cells embryonically and as Reelin[+]Prox1^{−} cells postnatally (arrowheads).

Schuman et al., 2021; Williams and Holtmaat, 2019) as well as GABAergic interneurons, together contributing to regulate the excitation/inhibition (E/I) balance (Anastasiades et al., 2021; Cohen-Kashi Malina et al., 2021; Fan et al., 2020; Genescu and Garel, 2021; Gesuita and Karayannis, 2021; Hartung and Letzkus, 2021; Ibrahim et al., 2016, 2020, 2021). Increasing evidence points toward a role of L1 in integrating top-down inputs, with the bottom-up thalamic inputs driven by external stimulation (Cauller, 1995; Schuman et al., 2021). Consistently, stimuli integration in apical dendrites of pyramidal neurons is a key feature for learning, plasticity, and cross-modal communication (Abs et al., 2018; Doron et al., 2020; Fan et al., 2020; Gambino et al., 2014; Ibrahim et al., 2016, 2020; Keller and Mrsic-Flogel, 2018; Larkum, 2013; Manita et al., 2015; Poorthuis et al., 2018; Shin et al., 2021; Suzuki and Larkum, 2020; Takahashi et al., 2016). In particular, apical dendrite activity in L5 pyramidal output neurons has been tightly linked with sensory perception (Manita et al., 2017; Schuman et al., 2021; Takahashi et al., 2016, 2020). Nonetheless, in spite of the physiological relevance of L1 for cortical functioning, we have a limited comprehension of the mechanisms regulating its development.

The embryonic and postnatal L1 hosts transient Cajal-Retzius cells (CRc). CRc are glutamatergic early-born neurons, best known for their roles in lamination and the production of the secreted glycoprotein Reelin (D'Arcangelo et al., 1995; Kirischuk et al., 2014; Tissir et al., 2009). CRc are produced by focal sources, migrate tangentially, and tile the neocortical surface, in part via contact repulsion (Barber et al., 2015; Barber and Pierani, 2016; Bielle et al., 2005; Causeret et al., 2021; Griveau et al., 2010; Ruiz-Reig et al., 2017; Villar-Cerviño et al., 2013; Yoshida et al., 2006). CRc undergo postnatal apoptosis in the neocortex, until their almost complete elimination by postnatal day (P) 25 (Blanquie et al., 2017; Causeret et al., 2018; Ledonne et al., 2016). Intriguingly, before their elimination, subsets of CRc redistribute by migration from the olfactory cortex into the neocortex, thereby maintaining CRc density at the surface of the growing neocortex (de Frutos et al., 2016). Both the embryonic redistribution and postnatal elimination of CRc were recently shown to be in part activity dependent and CRc density was proposed to regulate L1 development (de Frutos et al., 2016; Riva et al., 2019). However, which inputs contribute to CRc redistribution and what are their roles in L1 development remain largely to be addressed.

Here, by combining mouse genetics, manipulations of thalamic activity, and imaging, we reveal an interplay between spontaneous thalamic activity and transient CRc in the construction of L1. We show that prenatal spontaneous thalamic activity and NMDA receptors (NMDAR) control CRc embryonic densities

without affecting their activity-dependent apoptosis. Reduction in CRc density triggered long-lasting wiring deficits, with changes in the distribution of upper layer interneurons and in apical dendrite spines of L5 output pyramidal neurons. Consistently, reducing CRc density led to profound changes in apical dendrite activity in response to sensory stimulation. In contrast, early postnatal sensory deprivation selectively reduced basal dendrite spines of L5 output pyramidal neurons. Collectively, our results highlight an underappreciated role of prenatal thalamic activity onto embryonic transient CRc, which, in turn, regulate major features of L1 postnatal construction. Spontaneous bottom-up activity therefore has a long-term impact on the coordinated development of upper layers via superficial and transient guidepost CRc. Our study thus reveals important crosstalk between the development of bottom-up and top-down circuits as well as novel roles of spontaneous activity, with major implications for our comprehension of normal and pathological mechanisms of cortical wiring.

RESULTS

Prenatal spontaneous thalamic activity regulates early CRc density

CRc play key roles in L1 development, and their embryonic distribution and postnatal elimination are in part regulated by neuronal activity (Blanquie et al., 2017; de Frutos et al., 2016; Riva et al., 2019). Thalamic input is a main driver of cortical activity throughout development, starting with prenatal spontaneous waves that progress to asynchronous activity in sensory circuits and ultimately sensory-evoked activity (Antón-Bolaños et al., 2019; De Marco García et al., 2011; Erzurumlu and Gaspar, 2012; Iwasato et al., 2000; Jabaudon and López Bendito, 2012; López-Bendito and Molnár, 2003; Mizuno et al., 2018; Molnár et al., 2020; Moreno-Juan et al., 2017). We thus explored the role of thalamic activity on CRc density across their lifespan, focusing on the somatosensory cortex.

To this aim, we characterized CRc postnatal dynamics in this cortical region using two different strategies (Figures 1A and S1). We unambiguously labeled CRc by taking advantage of the $\Delta Np73^{cre/+}$ mouse line, which targets approximately 80% of CRc (Tissir et al., 2009) (Figures 1A and S1A). We also identified postnatal CRc as Reelin$^+$/Prox1$^-$ cells, since the Reelin protein is detected postnatally in some Prox1$^+$ interneurons (Tremblay et al., 2016) (Figure S1). Both methods highlight that postnatal CRc density, which results from migration and embryonic redistribution (Bielle et al., 2005; de Frutos et al., 2016; Ruiz-Reig et al., 2017; Tissir et al., 2009), is stable until P7 and sharply drops between P7 and P9 in the somatosensory cortex

(G) Quantification of CRc density (cells/mm of L1 length) reveals a phenotype similar to the one observed in (D) (E18.5: n = 5 controls, n = 4 mutants; P7: n = 3 controls, n = 5 mutants; P9: n = 3 controls, n = 3 mutants; and P15: n = 3 controls, n = 3 mutants).
(H) Schematic representation of the postnatal whisker pluck (WP) procedure (left).
(I) Confocal images of sections across the barrel cortex of $\Delta Np73^{cre/+};R26^{mT/+}$ at P7, P9, and P15 in controls and WP conditions immunostained for DsRed (red) to label CRc.
(J) Quantification of CRc density (cells/mm length of L1) shows no differences in controls and WP pups (right) (P7: n = 6 controls, n = 3 WP; P9: n = 4 controls, n = 3 WP; and P15: n = 4 controls, n = 3 WP).
Values are expressed as means ± SEMs, *p < 0.05; **p < 0.01; ***p < 0.001; 2-way ANOVA test with Sidak's multiple comparison correction. Scale bar represents 100 μm.

(Figure 1A and S1B). This drop corresponds to an activity-dependent apoptosis of some CRc (Blanquie et al., 2017; Ledonne et al., 2016; Riva et al., 2019) and is followed by a linear decrease until P25, likely due to a combination of elimination and dilution in a growing neocortical sheet (Figures 1A and S1).

To investigate the roles of prenatal thalamic activity in CRc distribution, we took advantage of a Cre-dependent mouse line that overexpresses the hyperpolarizing Kir2.1 channel ($R26^{Kir2.1/+}$; Moreno-Juan et al., 2017) backcrossed with two different thalamic drivers: (1) the $Gbx2^{creERT2/+}$ line (Chen et al., 2009), which targets most thalamic nuclei from the early embryonic stages when tamoxifen is injected at embryonic day (E)10.5 (Antón-Bolaños et al., 2019; Moreno-Juan et al., 2017) and (2) the $Sert^{cre/+}$ line (Zhuang et al., 2005), which targets mainly sensory thalamic nuclei from the late embryonic stages (Antón-Bolaños et al., 2019; Moreno-Juan et al., 2017) (Figures 1B–1G). Kir2.1 expression in both models was shown to in a timely manner eliminate spontaneous waves of thalamic activity without altering asynchronous activity (Moreno-Juan et al., 2017), and we found that these manipulations did not alter early CRc density at E13.5 (data not shown). By contrast, we found in both models that CRc density in the somatosensory barrel field (S1bf) was decreased by approximately 30% from late embryonic stages until P7 (Figures 1D–1G), and came back to normal levels at P9, after the peak CRc elimination. These findings indicate that prenatal thalamic activity regulates CRc embryonic density, with an impact on their density during the first postnatal week.

To next assess the role of postnatal thalamic sensory activity in CRc density and elimination, we performed postnatal deprivation induced by bilateral whisker plucking (WP) from P1 to P3 (Rhoades et al., 1990) (Figure 1H). This procedure impairs whisker-driven sensory stimulation and thalamic activity until whiskers regrow but does not affect the formation of barrels in the somatosensory cortex (Rhoades et al., 1990). We also performed unilateral infraorbital nerve lesion (ION), which blocks sensory activity from the whisker pad, severely impairs thalamic activity and barrel formation in the contralateral neocortex (Frangeul et al., 2014, 2016) (Figure S1C). In both models, we could not observe differences in the time course of CRc density and postnatal elimination (Figures 1H–1J and S1C). These results reveal that sensory activity relayed by the thalamus is not a main driver of CRc elimination occurring at the beginning of the second postnatal week (Riva et al., 2019; Ledonne et al., 2016).

Altogether, our work shows that prenatal thalamic waves regulate CRc early distribution, whereas postnatal thalamic activity has no detectable impact on their postnatal density or elimination.

NMDARs regulate prenatal and early postnatal CRc density

To further assess the role of excitatory activity in CRc early distribution, we examined the cell-autonomous roles of NMDARs by using a $GluN1^{flox}$ allele backcrossed with the $\Delta Np73^{cre/+}$ line (Figure 2). Indeed, it had been proposed that NMDARs contribute to regulate CRc neocortical density at embryonic stages, potentially by regulating the remigration of CRc from an olfactory reservoir near the lateral olfactory tract (LOT) (de Frutos et al., 2016). In conditional CRc-specific knockouts

(cKOs) of the GluN1 gene, which encode an essential subunit of NMDARs, we confirmed a 30% prenatal decrease in CRc density in the barrel cortex of cKO starting after E13.5 (de Frutos et al., 2016) and found that this decrease was maintained at postnatal stages (Figure 2A). Furthermore, by fate mapping in $\Delta Np73^{cre/+};GluN1^{fl/fl};R26^{mT/+}$ mice, we revealed that the decrease in CRc density in the P7 S1bf correlated with a converse 2.5-fold increase in CRc density in an olfactory reservoir near the LOT (Figure 2B). These results collectively reinforce the fact that NMDAR signaling in CRc regulates their redistribution across cortical regions. Using the same genetic model, we found no effect of GluN1 inactivation on the timing or efficiency of CRc elimination (Figure 2C).

Thus, both prenatal thalamus activity and GluN1 signaling regulate early activity-dependent CRc distribution, but not their postnatal elimination. Since thalamic inputs have not reached L1 at these early prenatal stages, they likely act through non-synaptic or multi-synaptic relays. Nonetheless, our results thus highlight a previously unsuspected role of prenatal synchronous thalamic waves and NMDAR signaling in the regulation of embryonic, and hence postnatal, CRc density. Since both CRc density and thalamic activity were proposed to influence L1 development and maturation, we examined the relative postnatal contribution of CRc and sensory-evoked activity.

Postnatal sensory activity and CRc regulate early L1 formation

To untangle the relative roles of CRc and sensory activity on the construction of L1 during the first postnatal week, we used two distinct models. We used sensory deprivation triggered by bilateral WP to selectively alter sensory-evoked activity without inducing major changes in cortical development or CRc density (Figures 1C, S2A, and S2B). For CRc density, we took advantage of the $\Delta Np73^{cre/+};R26^{dt-a/+}$ model, which drives the expression of a diphtheria toxin, leading to a 30% reduction in CRc density at embryonic stages and birth and a 45% reduction at P7 (Figure S2).

We focused on L1 thickness and on the numbers of Prox1+ interneurons derived from the preoptic area and caudal ganglionic eminence (POA/CGE), since we previously reported that CRc density regulates these two features in the first postnatal week (de Frutos et al., 2016). We found that either a WP-induced sensory deprivation or a reduced CRc density triggered similar phenotypes, including a reduction in L1 thickness and an increase in Prox1+ interneurons in the upper cortical layers, without drastic modifications in upper layer identity and barrel organization (Figure S2). To further assess whether activity-dependent changes in CRc density triggered similar changes in L1 development, we examined $\Delta Np73^{cre/+};GluN1^{fl/fl}$ mice (Figure S2). We found very similar changes, thereby highlighting that both CRc density and postnatal sensory activity act on L1 development during the first postnatal week.

Long-term roles of postnatal sensory activity and CRc on L1 wiring

Both postnatal sensory deprivation and decreased CRc density perturbed L1 formation during the first postnatal week, prompting us to investigate the long-term consequences on cortical
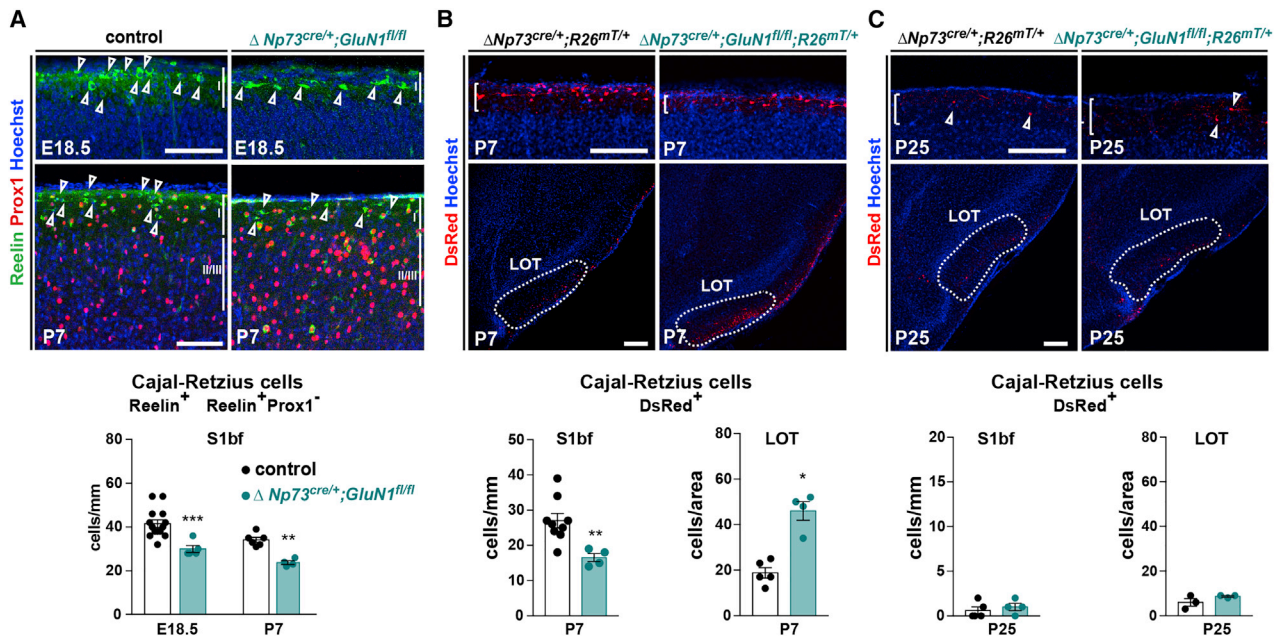
Figure 2. CRc density is maintained through a *GluN1*-dependent distribution and a *GluN1*-independent elimination

(A) Confocal images of coronal sections in the barrel cortex (S1bf) of E18.5 and P7 controls and *ΔNp73^{cre/+};GluN1^{fl/fl}* mutants. CRc are identified at embryonic stages as Reelin^{+} cells and postnatally as Reelin[+]Prox1^{−} cells (top). Quantification of CRc density (cells/mm of L1 length) (E18.5: n = 14 for controls, n = 5 for mutants; P7: n = 6 for controls, n = 4 for mutants) (bottom).

(B) Confocal images of coronal sections in the barrel cortex (S1bf) and lateral olfactory tract (LOT) of P7 *ΔNp73^{cre/+};R26^{mT/+}* controls and *ΔNp73^{cre/+};GluN1^{fl/fl};R26^{mT/+}* mutants. White brackets delineate L1, and the dotted line highlights the LOT (top). Quantification of CRc density L1 S1bf (cells/mm) and in the LOT (cells/area LOT, see Methods details) (bottom) (L1: n = 9 controls, n = 4 mutants; LOT: n = 5 controls, n = 4 mutants).

(C) Confocal images of coronal sections in the barrel cortex (S1bf) (top) and LOT (bottom) of P25 controls and *ΔNp73^{cre/+};GluN1^{fl/fl};R26^{mT/+}* mutants. White brackets delineate L1, and the dotted line highlights the LOT (top). Quantification of CRc density in L1 (cells/mm) and in the LOT (cells/area lot) (bottom) (L1: n = 5 controls, n = 4 mutants; LOT: n = 3 controls, n = 3 mutants).
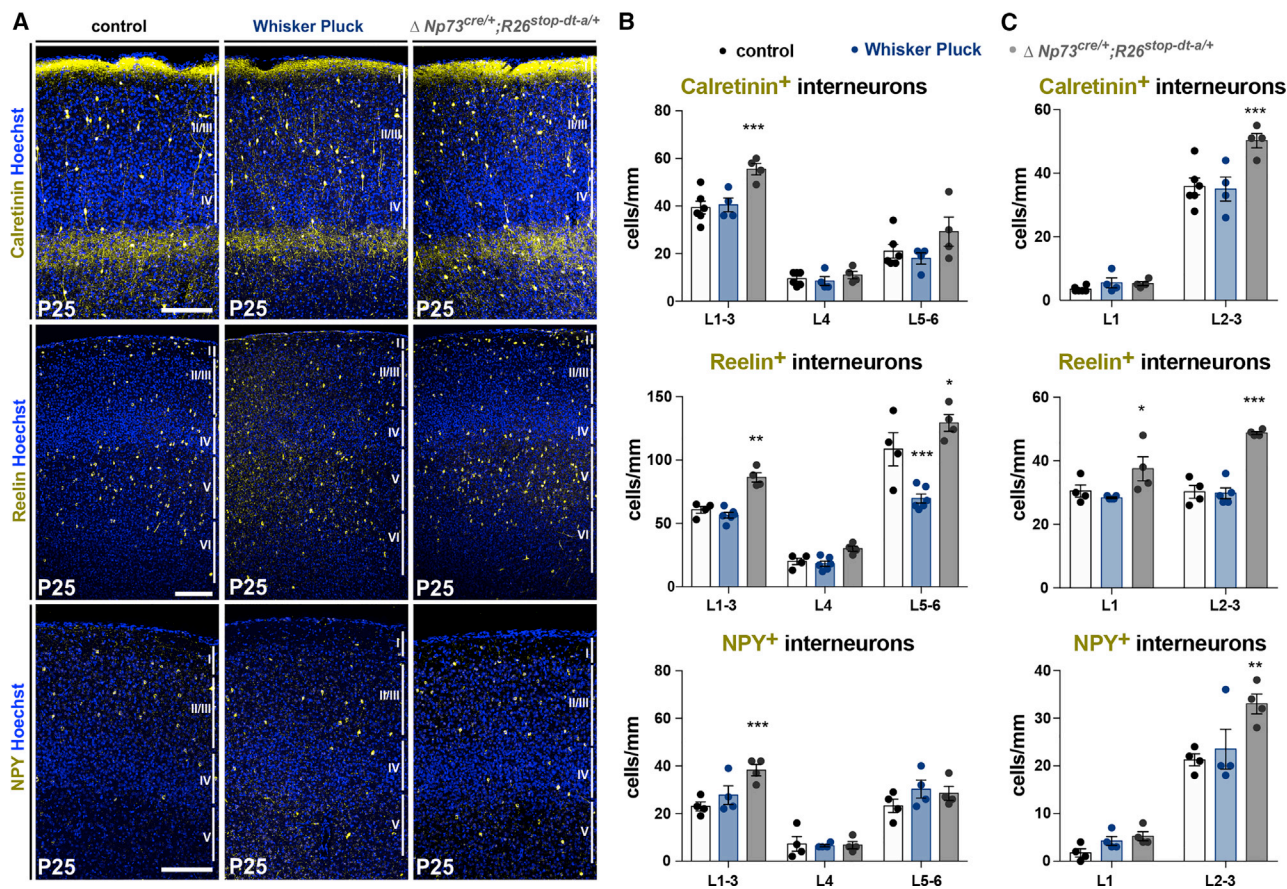
Values are expressed as means ± SEMs, 2-way ANOVA test with Sidak's multiple comparison correction in (A) and Mann-Whitney *U* tests in (B and C). *p < 0.05; **p < 0.001; ***p < 0.0001. Scale bars represent 100 μm in (A) and 200 μm in (B and C).

wiring. We focused on major functional features of the mature L1, namely interneurons and excitatory entries onto the apical dendrites of L5 pyramidal output neurons.

To this aim, we examined the distribution of subtypes of cortical interneurons that arise from POA/CGE-derived Prox1^{+} interneurons, since they were specifically affected at P7 (Figure S2). Prox1^{+} interneurons include a variety of interneurons that can directly regulate L1 entries, apical dendrite activity, or mediate disinhibition by acting on other interneurons (Fan et al., 2020; Miyoshi et al., 2015; Schuman et al., 2018). We focused on L2/3 Calretinin[+] bipolar interneurons as well as on subpopulations of Reelin[+] interneurons present in L1 and L2/3, combined with neuropeptide Y (NPY) to identify neurogliaform (NGF) cells (Gesuita and Karayannis, 2021; Niquille et al., 2018; Schuman et al., 2018). These classes of interneurons are essential to modulate information arriving in L1 or disinhibiting pyramidal neuron activity (Abs et al., 2018; Belén Pardi et al., 2020; Ibrahim et al., 2021; Larkum, 2013; Letzkus et al., 2011, 2015; Palmer et al., 2010). Both Reelin and Calretinin are also expressed in CRc, but these cells have mostly disappeared by P25, enabling us to use these markers to selectively label interneuron subpopulations (Figures S1 and S3). We found that sensory deprivation triggered by postnatal WP did not induce major

changes in the distribution of upper layer interneurons (Figures 3A–3C). By contrast, *ΔNp73^{cre/+};R26^{dt-a/+}* mice presented a marked increase in the densities of Calretinin[+] bipolar interneurons and NGF cells as revealed by Reelin and NPY immunostaining (Figures 3A–3C). We also examined the impact of sensory deprivation and reduced CRc density on the distribution of other populations of interneurons derived from the medial ganglionic eminence (MGE), namely PV[+] and SST[+], since sensory activity had already been proposed to shape their distribution (Modol et al., 2020; Tremblay et al., 2016). We found in both models a selective decrease in deep layer PV[+] interneurons (Figure S3), which could be accounted for by overall changes in cortical activity. Taken together, our analysis reveals that, in contrast to sensory deprivation, a reduction in CRc density has a long-term impact on the densities of both bipolar and NGF cells, two populations that can respectively act as mediators of disinhibition or inhibition (Armstrong et al., 2012; Bartolini et al., 2013; Fan et al., 2020; Huang and Paul, 2019; Ibrahim et al., 2021; Schuman et al., 2018; Tremblay et al., 2016).

To further assess the excitatory entries in L1, we took advantage of the *Thy1::YFP* reporter line (Feng et al., 2000) that sparsely labels L5 pyramidal neurons, the main output cortical neurons (Harris and Shepherd, 2015). In both conditions, the
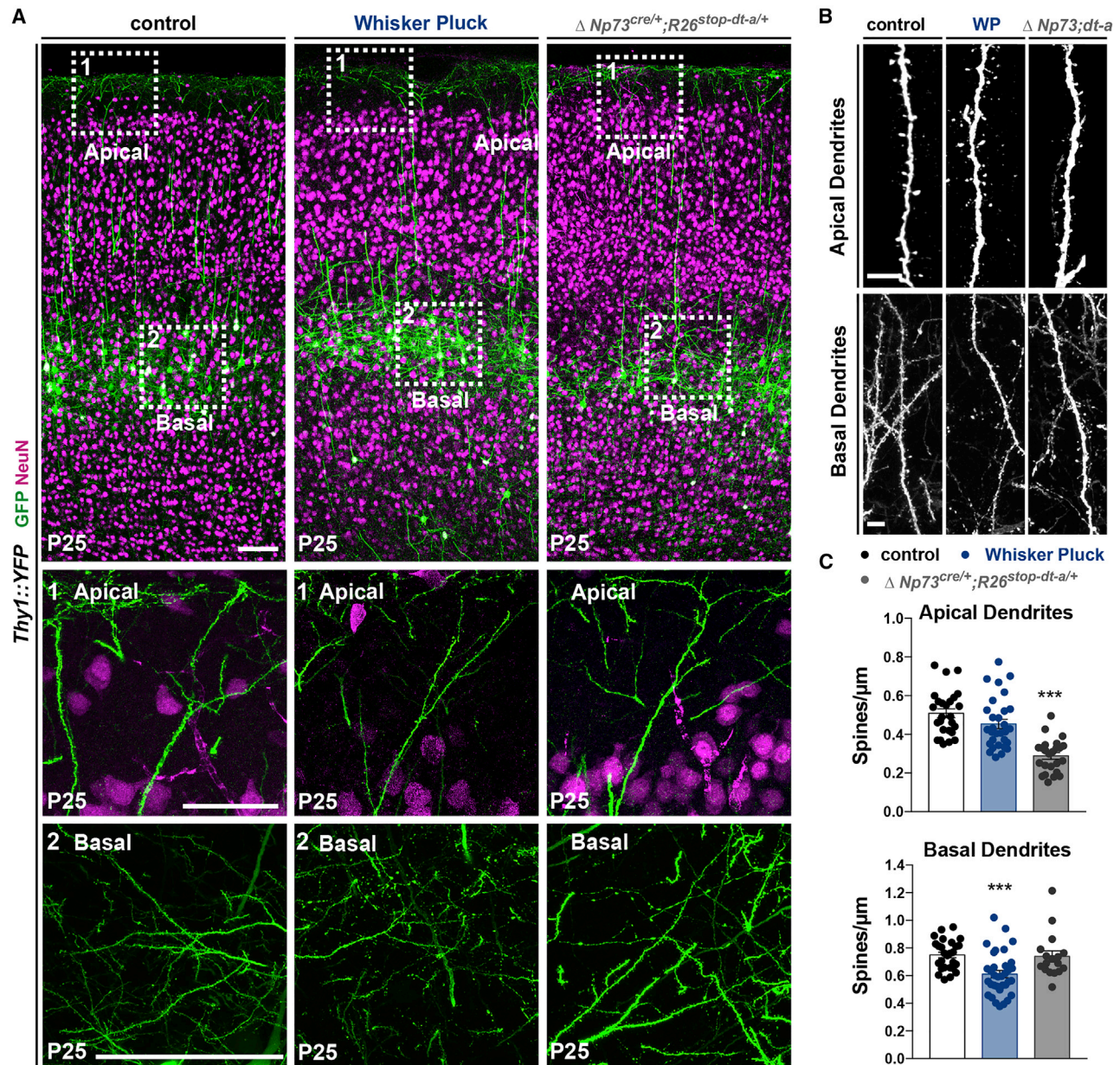
Figure 4. Sensory deprivation and decrease in CRc density selectively modify spines of basal or apical dendrites

(A) Confocal images of coronal sections in the somatosensory cortex of P25 controls, animals that were postnatally WP and $\Delta Np73^{cre/+};R26^{dt-a/+}$ mutants, all expressing the *Thy1::YFP* allele, which enables one to sparsely label L5 pyramidal neurons. The whole cortical thickness is presented in the top panels with NeuN immunostaining, with close-ups on L1 apical dendrites (center) and close-ups on basal dendrites (bottom).

(B) Confocal images of spines on apical (top) and basal (bottom) dendrites of L5 pyramidal neurons in control, WP, and $\Delta Np73^{cre/+};R26^{dt-a/+}$ mutants.

(C) Quantifications of the spine density on the apical (top) and basal (bottom) dendrites of L5 pyramidal neurons (apical dendrites were examined in n = 4 control mice, n = 5 WP, and n = 3 $\Delta Np73^{cre/+};R26^{dt-a/+}$ mutants).

Values are expressed as means ± SEMs, Kruskal-Wallis multiple comparison test. *p < 0.05; **p < 0.001; ***p < 0.0001. Scale bars represent 100 μm in (A) and 5 μm in (B).

activity-dependent apoptosis (Riva et al., 2019). We thus overexpressed excitatory designer receptors exclusively activated by designer drugs (DREADDs) in CRc $(\Delta Np73^{cre/+}R26^{DR/+})$ and stimulated them from P1 to P3 with clozapine N-oxide (CNO) injections, as we did for controls (Figure 5A). This procedure led to

a premature CRc elimination during the first postnatal week, reaching a 30% decrease by P7 (Figures 5A–5C). This temporally controlled manipulation recapitulated specific aspects of the phenotypes observed in the $\Delta Np73^{cre/+};R26^{dt-a/+}$ model (Figures 5, S2, and S4). We observed a similar increase in
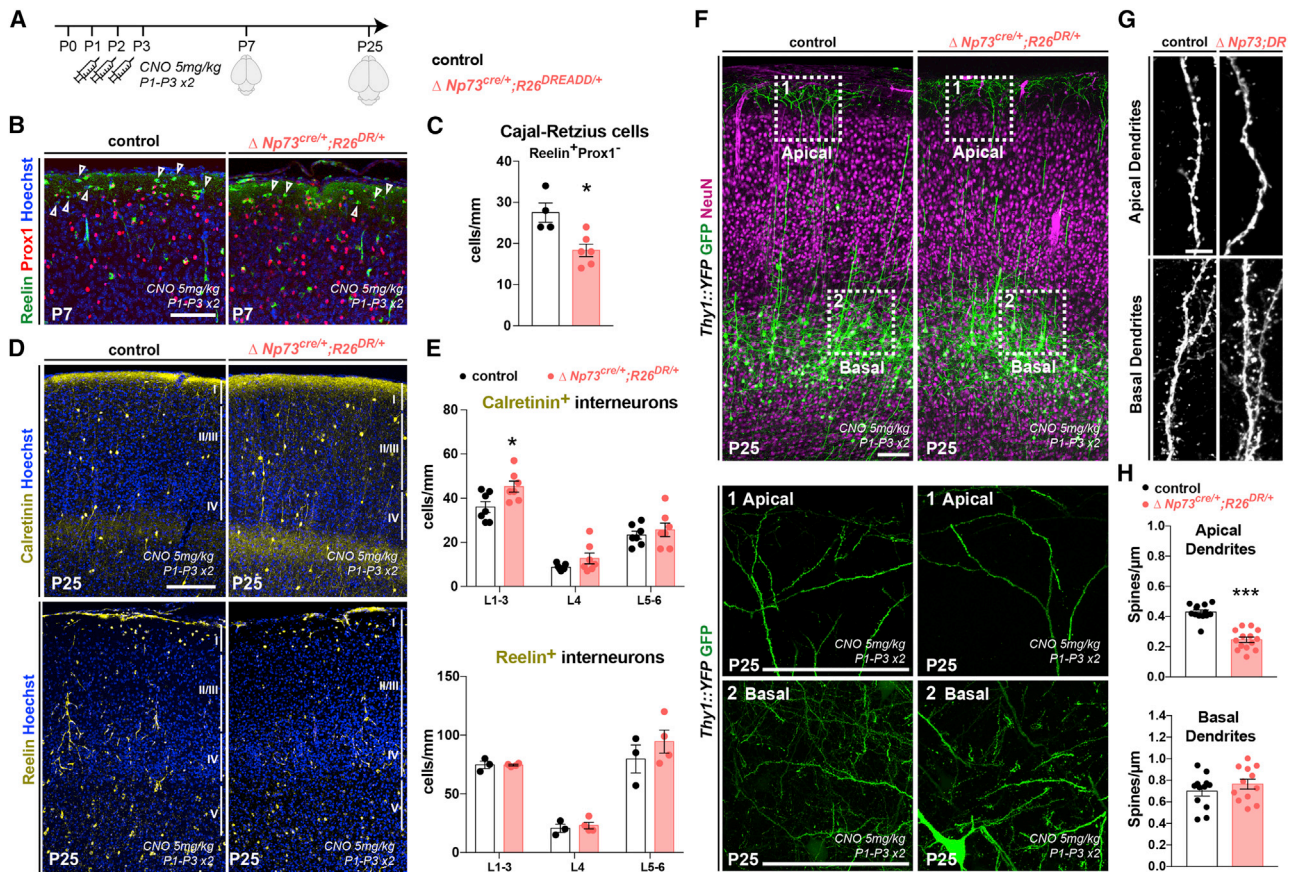
Figure 5. Postnatal reduction in CRc regulates apical dendrite spine density and Calretinin⁺ interneuron distribution

(A) Schematics of the strategy used to prematurely eliminate some CRc by overactivation using 2 daily CNO injections from P1 to P3 in $\Delta Np73^{cre/+};R26^{DREADD/+}$ mutants ($\Delta Np73^{cre/+};R26^{DR/+}$) and control littermates.

(B) Confocal images of coronal sections in the barrel cortex (S1bf) of P7 controls and $\Delta Np73^{cre/+};R26^{DR/+}$ mutants animals in which CRc are identified as L1 Reelin⁺Prox1⁻ cells (arrowheads).

(C) Quantification of CRc density (cells/mm of L1 length) (n = 4 for controls and n = 6 for mutants), showing that CRc overactivation drives their premature elimination by P7.

(D) Confocal images of coronal sections in the barrel cortex of P25 controls and $\Delta Np73^{cre/+};R26^{DR/+}$ mutants immunostained for Calretinin and Reelin to identify subgroups of POA/CGE-derived interneurons.

(E) Quantifications of interneuron density in upper cortical layers (L1–3), L4, and deep cortical layers (L5–6), showing that the overactivation of CRc and their premature elimination selectively increases the density of Calretinin⁺ and Reelin⁺ interneurons (Calretinin: n = 7 for controls, n = 7 for mutants; Reelin: n = 3 for controls, n = 4 for mutants).

(F) Confocal images of coronal sections in the barrel cortex of P25 controls and $\Delta Np73^{cre/+};R26^{DR/+}$, all expressing the *Thy1::YFP* allele. The whole cortical thickness is presented in the top panels, with close-ups on L1 apical dendrites (ceenter) and close-ups on basal dendrites (bottom).

(G) Confocal images of spines on the apical (top) and basal (bottom) dendrites of L5 pyramidal neurons in controls and $\Delta Np73^{cre/+};R26^{DR/+}$ mutants.

(H) Quantifications of the spine density on the apical (top) and basal (bottom) dendrites of L5 pyramidal neurons, showing a selective reduction in apical spine density in the experimental condition (n = 3 for controls and n = 3 for $\Delta Np73^{cre/+};R26^{DR/+}$ mutants).

Values are expressed as means ± SEMs, Mann-Whitney test in (C) and (H), and 2-way ANOVA test with Sidak's multiple comparison correction in (E). *$p < 0.05$; **$p < 0.001$; ***$p < 0.0001$. Scale bars represent 200 μm in (B), 200 μm in (D), 100 μm in (F), and 5 μm in (G).

Prox1⁺ and Calretinin⁺ interneurons at P7, whereas postnatal CRc manipulations led to a similar increase in Calretinin⁺ bipolar interneurons but no changes in the density of Reelin⁺ NGF cells (Figures 5, S4A, and S4B). This partial phenocopy reveals that CRc likely have both an embryonic and a postnatal impact on interneuron development, with a global prenatal effect on Prox1⁺ cells and a more specific postnatal influence on Calretinin⁺ bipolar interneurons. Regarding apical dendrites, the $\Delta Np73^{cre/+}R26^{DR/+}$ model recapitulated the defects observed in the $\Delta Np73^{cre/+}R26^{dta}$ model at P25 (Figure 5),

thereby highlighting the postnatal role of CRc on spine development in L1.

Collectively, our experiments reveal major functions of CRc density on L1 wiring during the first postnatal week, putting forward distinct roles that these transient cells display across specific developmental phases.

CRc density shapes L1 apical dendrite activity
The overall anatomical changes induced by CRc reduced density raises the question of the potential functional consequences
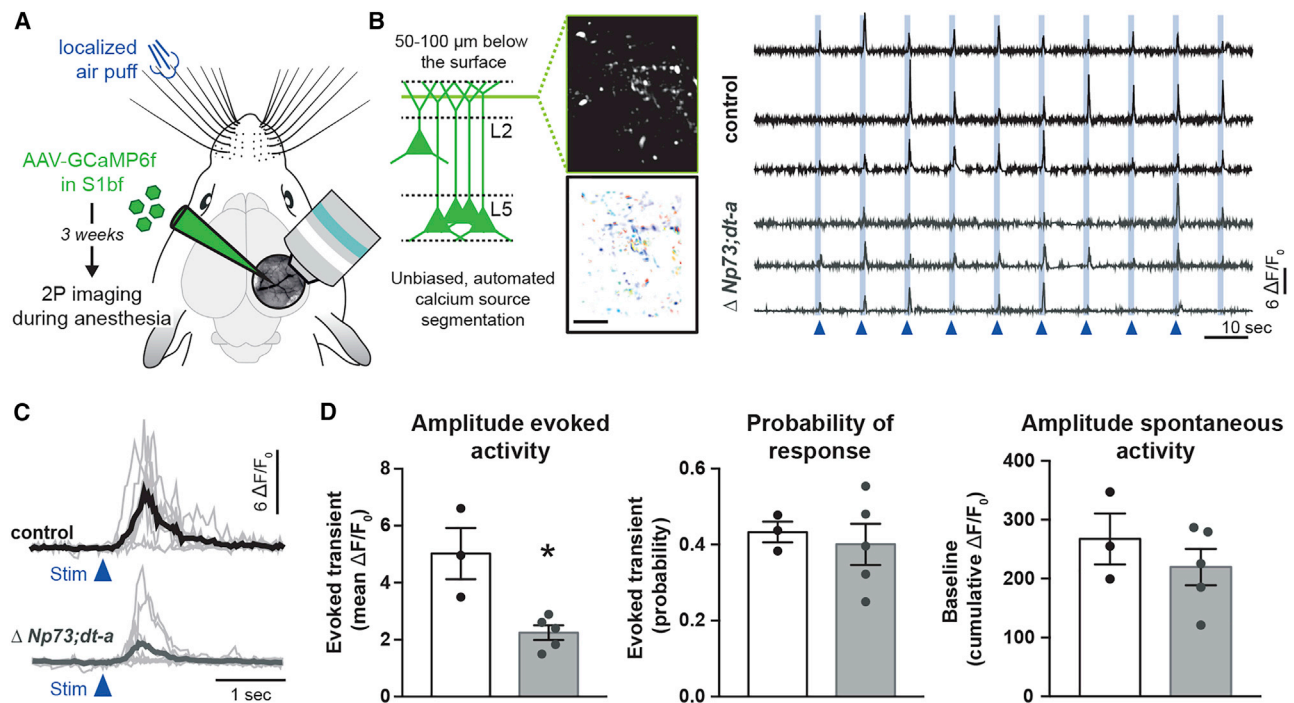
Figure 6. CRc density controls the activity of apical dendrites in L1

(A) Schematics of the experimental strategy. L5 pyramidal neurons were transfected with adeno-associated virus (AAV)-GCaMP6f and their dendrites were imaged in L1 of the barrel cortex through a cranial window, in response to whisker deflections during isoflurane anesthesia.

(B) Two-photon Ca^{2+} imaging from apical dendrites of L5 neurons in S1 expressing GCaMP6f. Fluorescence change was measured in Ca^{2+} sources that were automatically segmented (left). Example traces of calcium transients ($\Delta F/F_0$) in sources obtained from controls and $\Delta Np73^{cre/+};R26^{dt-a/+}$ mutants upon 10 whisker stimulations (right).

(C) Example traces of single whisker-evoked calcium transients from one typical calcium source in controls (top) and $\Delta Np73^{cre/+};R26^{dt-a/+}$ mutants (bottom) mice.

(D) Quantifications of the evoked amplitude showing a selective reduction in apical spine density in the experimental condition (n = 3 controls and n = 5 $\Delta Np73^{cre/+};R26^{dt-a/+}$ mutants).

Values are expressed as means ± SEMs, Mann-Whitney test. Scale bars represent 20 μm in (B).

on the *in vivo* activity of apical tufts in L1. Indeed, while an increase in NGF cells and a reduction in apical spine density could be linked to decreased apical dendrite activity, the observed increase in Calretinin$^+$ bipolar cells could have indirect and not easily predictable influences. To directly assess apical tuft activity, we used adeno-associated virus (AAV) vectors to express the genetically encoded Ca^{2+} indicator GCaMP6f in L5 pyramidal neurons in the C2 barrel column in S1bf (Gambino et al., 2014; Takahashi et al., 2016). We imaged with two-photon microscopy Ca^{2+} responses in putative L5 apical dendritic tufts in L1 through a chronically implanted cranial window, while single whiskers were deflected with calibrated air puffs (Figure 6A). Brief puffs of air were used to deflect preferentially the C2 principal whisker (10 stimulations, 0.1 Hz) (Figure 6A). Dendritic domains with asynchronous Ca^{2+} activity (i.e. Ca^{2+} sources) were automatically segmented by using a custom and unbiased source separation method based on the non-negative matrix factorization method after lateral and out-of-focus correction (Pnevmatikakis and Giovannucci, 2017; Pnevmatikakis et al., 2016). This procedure enabled us to assess fluorescent changes in these Ca^{2+} sources after automatically detecting them in each field of view (FOV) (Figure 6B), enabling us to identify on average 14.8 ± 6 and 16.8 ± 9 Ca^{2+} sources per FOV in respectively controls (n = 3 mice; 21 FOV; 339 sources) and $\Delta Np73^{cre/+};R26^{dt-a/+}$ mice (n = 5 mice; 28 FOV; 578 sources). In accordance with previous reports (Gambino et al., 2014; Takahashi et al., 2016), single whisker deflections evoke Ca^{2+} transients in most spines and dendritic shafts under light isoflurane anesthesia (Figures 6B and 6C). We found that, on average, evoked Ca^{2+} transients were significantly smaller in the $\Delta Np73^{cre/+};R26^{dt-a/+}$ model compared to controls (Figures 6C and 6D), which could be well explained by the decrease in dendritic spines, the increase in interneuron density, or a combination of both. In contrast, neither the probability of responsiveness nor the occurrence of spontaneous Ca^{2+} transients were affected by a decreased CRc density (Figure 6D), suggesting that presynaptic inputs were not altered. This indicates that a proper density of CRc during their lifetime regulates the appropriate apical dendritic integration of sensory inputs in adult animals.

Overall, our study reveals a remarkable interplay between CRc and sensory thalamus activity. Prenatal spontaneous thalamic activity regulates the embryonic density of CRc, which, in turn, regulates POA/CGE-derived interneuron distribution as well as, postnatally, synaptogenesis and functional integration on apical dendrites. Postnatal sensory activity relayed by the thalamus is conversely a major local regulator

of excitatory synaptogenesis on basal dendrites of output pyramidal neurons of the neocortex.

DISCUSSION

L1 regulates top-down input integration and higher order functions such as perception, learning, arousal, and consciousness via an exquisite architecture (Doron et al., 2020; Suzuki and Larkum, 2020; Takahashi et al., 2016; Williams and Holtmaat, 2019). So far, we have a limited understanding of how L1 assembles, in particular in relationship to the wiring of bottom-up circuits relayed by thalamic sensory circuits that are well described, from prenatal spontaneous activity and subplate relay to sensory-evoked plasticity (Antón-Bolaños et al., 2019; Galazo, et al., 2008; Ghezzi et al., 2020; Kanold and Luhmann, 2010; Luhmann et al., 2018; Luhmann et al., 2016; Moreno-Juan et al., 2017; Ohtaka-Maruyama, 2020; Rubio-garrido et al., 2009) Here, we show that CRc act as a key intermediate between thalamic spontaneous activity and the development of major anatomical and functional features of L1. These findings highlight the multiple functions of CRc across development as well as the long-term impact of spontaneous activity on L1 circuit formation, with major implications for our comprehension of the mechanisms governing cortical wiring.

CRc have been shown or proposed to act at various stages of corticogenesis. From their prenatal roles in cortical lamination (Gil-Sanz et al., 2013; Kirischuk et al., 2014; Yoshida et al., 2006) or interneuron progression (Caronia-Brown and Grove, 2011), we and others recently revealed a role for CRc density on L1 development, including the morphogenesis of upper layer apical dendrites (de Frutos et al., 2016; Riva et al., 2019). In this study, we provide evidence that CRc density regulates excitatory synapse density on apical dendrites of deep layer neurons, as well as the number of different subsets of interneuron populations, including bipolar Calretinin^{+} neurons and upper layer Reelin^{+} NGF cells, that can respectively contribute to disinhibition or inhibition (Armstrong et al., 2012; Bartolini et al., 2013; Fan et al., 2020; Huang and Paul, 2019; Ibrahim et al., 2021; Schuman et al., 2018; Tremblay et al., 2016). Functionally, we found that decreased CRc density leads to a reduction in the activation of L5 apical dendrites in response to sensory stimulation in S1bf (Figure 6), a feature that is essential for cortical processing (Manita et al., 2015; Palmer et al., 2014; Suzuki and Larkum, 2020; Takahashi et al., 2016, 2020). These findings highlight that CRc, by orchestrating the development of both excitatory inputs and interneuron populations, act as major regulators of the apical circuits that in adults integrate top-down information, mirroring the roles of subplate cells in shaping cortical bottom-up circuits (Kanold and Luhmann, 2010; Ohtaka-Maruyama, 2020). Furthermore, by taking advantage of their sensitivity to electrical activity, we could disentangle prenatal and postnatal roles of CRc. We found that eliminating CRc prematurely during the first postnatal week (Figures 5 and S4) selectively phenocopied the impact of CRc density reduction for apical dendrite spines and the distribution of Calretinin[+] bipolar interneurons (Figure 3). Altogether, our study underlines the specific contribution of postnatal CRc onto L1 wiring and delineates distinct prenatal and postnatal functions, for instance, on different inter-

neuron subpopulations. Our work furthermore points to a major role for CRc on the development of both excitatory inputs and inhibitory circuits, with coordinated anatomical and functional consequences.

Orchestrating roles of CRc are tightly regulated by the spontaneous activity of the prenatal thalamus. Indeed, we found that selectively modifying the prenatal and not postnatal activity of the thalamus had a striking effect on the embryonic, and hence postnatal CRc density (Figures 1 and S1). This role is reinforced by the finding that similar phenotypes are observed in NMDAR CRc-specific mutants, in which olfactory CRc are increased at the expense of neocortical somatosensory CRc (Figure 2). It is important to stress that none of these experimental models affected CRc density at E13.5 (not shown), highlighting that the changes in CRc densities occur during the redistribution period that we previously identified (de Frutos et al., 2016). Since thalamic inputs are not directly in contact with L1 during embryonic development (Galazo et al., 2008; Kirischuk et al., 2014; Rubio-garrido et al., 2009), the effect of thalamic activity is likely indirect, via multiple cellular relays. The subplate, which was recently shown to host neurons that receive thalamic inputs and project to L1, constitutes a potential candidate for bridging the thalamus to the neocortical L1 at embryonic stages (Ghezzi et al., 2020; Hoerder-Suabedissen and Molnár, 2013; Luhmann et al., 2018; Meng et al., 2020; Myakhar et al., 2011; Ohtaka-Maruyama, 2020).

While the underlying mechanisms remain to be addressed, our study highlights an unsuspected function of prenatal thalamic spontaneous activity. We find that these early waves not only shape incoming bottom-up sensory inputs but also affect the formation of apical circuits that in adults integrate top-down information. While it was established that thalamic axons and their activity have an impact on many aspects of cortical wiring, it was mainly proposed that such impacts occur at postnatal stages (Anastasiades et al., 2021; Carter and Regehr, 2000; Ibrahim et al., 2021; Jabaudon et al., 2012; Li et al., 2013; Matsui et al., 2013). Recent studies revealed an unprecedented role for prenatal thalamic waves in columnar formation (Antón-Bolaños et al., 2019). Our current findings extend it to L1 and upper layers, thereby providing a "bridging" checkpoint for thalamic control of neocortical wiring at prenatal and postnatal stages. In addition, our findings indicate that by regulating the density of CRc, early spontaneous activity can have long-lasting effects on circuit wiring.

This feature contrasts with the current schema that cortical circuits wire in a linear manner, with first genetically controlled developmental programs, which are then shaped and refined by spontaneous activity and followed by evoked activity. Our study, together with previous work, put forward a recursive model of cortical development involving sequences. More specifically, CRc exert multiple functions at specific time points of their "short" lives: (1) they regulate neocortical lamination, interneuron distribution, and axonal navigation in the embryo (Causeret et al., 2021; Genescu and Garel, 2021; Gesuita and Karayannis, 2021; Kirischuk et al., 2014); (2) they are redistributed in an activity-dependent manner and their embryonic distribution relies on spontaneous activity of the thalamus; (3) CRc coordinately act upon key aspects of L1 development during postnatal development with long-term functional consequences; (4)

subsets of CRc are dismissed by an activity-dependent mechanism that remains to be characterized (Riva et al., 2019). All of these steps ensure the proper wiring of cortical circuits. Remarkably, all of these steps are driven by transient interactions, cell movements, and an interplay between different types of neuronal activity. During these phases, CRc exert distinct roles in the construction of cortical circuits, putting forward that through migration, activity, and elimination, transient interactions can endow cells with multiple functions across developmental sequences. Such a recursive scheme ensures the coordinated development of basal and apical dendrites of cortical neurons, and starts from prenatal stages. These findings have important implications for our understanding of cortical wiring but also of the etiology of neurodevelopmental disorders.

Collectively, our work establishes remarkable roles for early thalamic activity and transient cortical neurons in the formation of an essential but understudied layer of the neocortex and provides key insights into how transient changes during embryonic life remain imprinted in neocortical networks.

Limitations of the study

A limitation of our study is the lack of dissection of the microcircuits conveying spontaneous thalamic activity to CRc. A tempting hypothesis is that subplate cells or deep layer interneurons that receive thalamic inputs could, in turn, contact CRc (Cocas et al., 2016; Kanold and Luhmann, 2010; Luhmann et al., 2016; Meng et al., 2020; Molnár et al., 2020; Myakhar et al., 2011). However, the *in vivo* evidence for this direct connection between the subplate and CRc is still missing and could be addressed in future studies, for instance by *trans*-synaptic rabies viral tracing and functional *in vivo* experiments. Another limitation of our study is that we focused on a single cortical area, the barrel cortex, and we did not explore the potential functional heterogeneity of CRc that were shown to originate from distinct sources (Barber and Pierani, 2016; Causeret et al., 2021). It would be important to explore whether the roles that we have highlighted are conserved across cortical regions and all CRc, to evaluate the possible generalization of our findings for the wiring of all of the neocortical sheet. Finally, our assessment of apical dendrite activity was performed in anesthetized animals, which reduces overall activity patterns (Suzuki and Larkum, 2020). Our observations of decreased apical dendritic activity nonetheless reveal that CRc reduction induces a major structural long-term alteration in the circuit that may trigger enhanced abnormal responses in the context of awake-behaving animals.

Regardless of these limitations and others that are discussed throughout the manuscript, our study adds to the growing body of evidence that transient cells and transient patterns of spontaneous activity in development have a major and long-lasting impact on cortical circuit wiring.

STAR★METHODS

Detailed methods are provided in the online version of this paper and include the following:

REFERENCES

Abs, E., Poorthuis, R.B., Apelblat, D., Muhammad, K., Pardi, M.B., Enke, L., Kushinsky, D., Pu, D.L., Eizinger, M.F., Conzelmann, K.K., et al. (2018). Learning-related plasticity in dendrite-targeting layer 1 interneurons. Neuron *100*, 684–699.e6.

Ackman, J.B., and Crair, M.C. (2014). Role of emergent neural activity in visual map development. Curr. Opin. Neurobiol. *24*, 166–175.

Ackman, J.B., Burbridge, T.J., and Crair, M.C. (2012). Retinal waves coordinate patterned activity throughout the developing visual system. Nature *490*, 219–225.

Anastasiades, P.G., Collins, D.P., and Carter, A.G. (2021). Mediodorsal and ventromedial thalamus engage distinct L1 circuits in the prefrontal cortex. Neuron *109*, 314–330.e4.

Antón-Bolaños, N., Sempere-ferràndez, A., Guillamón-Vivancos, T., Martini, F.J., Pérez-Saiz, L., Gezelius, H., Filipchuk, A., Valdeolmillos, M., and López-bendito, G. (2019). Prenatal activity from thalamic neurons governs the emergence of functional cortical maps in mice. Science *364*, 987–990.

Armstrong, C., Krook-Magnuson, E., and Soltesz, I. (2012). Neurogliaform and Ivy cells: a major family of nNOS expressing GABAergic neurons. Front. Neural Circuits *6*, 23.

Arroyo, D.A., and Feller, M.B. (2016). Spatiotemporal features of retinal waves instruct the wiring of the visual circuitry. Front. Neural Circuits *10*, 54.

Babola, T.A., Li, S., Gribizis, A., Lee, B.J., Issa, J.B., Wang, H.C., Crair, M.C., and Bergles, D.E. (2018). Homeostatic control of spontaneous activity in the developing auditory system. Neuron *99*, 511–524.e5.

Barber, M., and Pierani, A. (2016). Tangential migration of glutamatergic neurons and cortical patterning during development: lessons from Cajal-Retzius cells. Dev. Neurobiol. *76*, 847–881.

Barber, M., Arai, Y., Morishita, Y., Vigier, L., Causeret, F., Borello, U., Ledonne, F., Coppola, E., Contremoulins, V., Pfrieger, F.W., et al. (2015). Migration speed of Cajal-Retzius cells modulated by vesicular trafficking controls the size of higher-order cortical areas. Curr. Biol. *25*, 2466–2478.

Bartolini, G., Ciceri, G., and Marín, O. (2013). Integration of GABAergic interneurons into cortical cell assemblies: lessons from embryos and adults. Neuron *79*, 849–864.

Belén Pardi, M., Vogenstahl, J., Dalmay, T., Spanò, T., Pu, D.L., Naumann, L.B., Kretschmer, F., Sprekeler, H., and Letzkus, J.J. (2020). A thalamocortical top-down circuit for associative memory. Science *370*, 844–848.

Bielle, F., Griveau, A., Narboux-Nême, N., Vigneau, S., Sigrist, M., Arber, S., Wassef, M., and Pierani, A. (2005). Multiple origins of Cajal-Retzius cells at the borders of the developing pallium. Nat. Neurosci. *8*, 1002–1012.

Blankenship, A.G., and Feller, M.B. (2010). Mechanisms underlying spontaneous patterned activity in developing neural circuits. Nat. Rev. Neurosci. *11*, 18–29.

Blanquie, O., Liebmann, L., Hübner, C.A., Luhmann, H.J., and Sinning, A. (2017). NKCC1-mediated GABAergic signaling promotes postnatal cell death in neocortical Cajal–Retzius cells. Cereb. Cortex. *27*, 1644–1659.

Brockschnieder, D., Pechmann, Y., Sonnenberg-Riethmacher, E., and Riethmacher, D. (2006). An improved mouse line for cre-induced cell ablation due to diphtheria toxin A, expressed from the Rosa26 locus. Genesis *45*, 76–82.

Callaway, E.M., and Borrell, V. (2011). Developmental sculpting of dendritic morphology of layer 4 neurons in visual cortex: influence of retinal input. J. Neurosci. *31*, 7456–7470.

Campelo, T., Augusto, E., Chenouard, N., de Miranda, A., Kouskoff, V., Camus, C., Choquet, D., and Gambino, F. (2020). AMPAR-dependent synaptic plasticity initiates cortical remapping and adaptive behaviors during sensory experience. Cell Rep. *32*, 108097.

Caronia-Brown, G., and Grove, E.A. (2011). Timing of cortical interneuron migration is influenced by the cortical hem. Cereb. Cortex. *21*, 748–755.

Carter, A.G., and Regehr, W.G. (2000). Prolonged synaptic currents and glutamate spillover at the parallel fiber to stellate cell synapse. J. Neurosci. *20*, 4423–4434.

Cauller, L. (1995). Layer I of primary sensory neocortex: where top-down converges upon bottom-up. Behav. Brain Res. *71*, 163–170.

Causeret, F., Coppola, E., and Pierani, A. (2018). Cortical developmental death: selected to survive or fated to die. Curr. Opin. Neurobiol. *53*, 35–42.

Causeret, F., Moreau, M.X., Pierani, A., and Blanquie, O. (2021). The multiple facets of Cajal-Retzius neurons. Development *148*, dev199409.

Che, A., Babij, R., Iannone, A.F., Fetcho, R.N., Ferrer, M., Liston, C., Fishell, G., and De Marco García, N.V. (2018). Layer I interneurons sharpen sensory maps during neonatal development. Neuron *99*, 98–116.e7.

Chen, L., Guo, Q., and Li, J.Y.H. (2009). Transcription factor Gbx2 acts cell-nonautonomously to regulate the formation of lineage-restriction boundaries ofthe thalamus. Development *136*, 1317–1326.

Cocas, L.A., Fernandez, G., Barch, M., Doll, J., Zamora Diaz, I., Pleasure, S.J., Diaz, I.Z., and Pleasure, X.J. (2016). Cell type-specific circuit mapping reveals the presynaptic connectivity of developing cortical circuits. J. Neurosci. *36*, 3378–3390.

Cohen-Kashi Malina, K., Tsivourakis, E., Kushinsky, D., Apelblat, D., Shtiglitz, S., Zohar, E., Sokoletsky, M., Tasaka, G.I., Mizrahi, A., Lampl, I., et al. (2021). NDNF interneurons in layer 1 gain-modulate whole cortical columns according to an animal's behavioral state. Neuron *109*, 2150–2164.e5.

Cossart, R. (2011). The maturation of cortical interneuron diversity: how multiple developmental journeys shape the emergence of proper network function. Curr. Opin. Neurobiol. *21*, 160–168.

Cruikshank, S.J., Ahmed, O.J., Stevens, T.R., Patrick, S.L., Gonzalez, A.N., Elmaleh, M., and Connors, B.W. (2012). Thalamic control of layer 1 circuits in prefrontal cortex. J. Neurosci. *32*, 17813–17823.

D'Arcangelo, G., Miao, G.G., Chen, S.C., Scares, H.D., Morgan, J.I., and Curran, T. (1995). A protein related to extracellular matrix proteins deleted in the mouse mutant reeler. Nature *374*, 719–723.

Doron, G., Shin, J.N., Takahashi, N., Drüke, M., Bocklisch, C., Skenderi, S., De Mont, L., Toumazou, M., Ledderose, J., Brecht, M., et al. (2020). Perirhinal input to neocortical layer 1 controls learning. Science *370*, eaaz3136.

Erzurumlu, R.S., and Gaspar, P. (2012). Development and critical period plasticity of the barrel cortex. Eur. J. Neurosci. *35*, 1540–1553.

Fan, L.Z., Kheifets, S., Böhm, U.L., Wu, H., Piatkevich, K.D., Xie, M.E., Parot, V., Ha, Y., Evans, K.E., Boyden, E.S., et al. (2020). All-optical electrophysiology reveals the role of lateral inhibition in sensory processing in cortical layer 1. Cell *180*, 521–535.e18.

Feng, G., Mellor, R.H., Bernstein, M., Keller-Peck, C., Nguyen, Q.T., Wallace, M., Nerbonne, J.M., Lichtman, J.W., and Sanes, J.R. (2000). Imaging neuronal subsets in transgenic mice expressing multiple spectral variants of GFP. Neuron *28*, 41–51.

Frangeul, L., Porrero, C., Garcia-Amado, M., Maimone, B., Maniglier, M., Clascá, F., and Jabaudon, D. (2014). Specific activation of the paralemniscal pathway during nociception. Eur. J. Neurosci. *39*, 1455–1464.

Frangeul, L., Pouchelon, G., Telley, L., Lefort, S., Luscher, C., and Jabaudon, D. (2016). A cross-modal genetic framework for the development and plasticity of sensory pathways. Nature *538*, 96–98.

de Frutos, C.A., Bouvier, G., Arai, Y., Thion, M.S., Lokmane, L., Keita, M., Garcia-Dominguez, M., Charnay, P., Hirata, T., Riethmacher, D., et al. (2016). Reallocation of olfactory Cajal-Retzius cells shapes neocortex architecture. Neuron *92*, 435–448.

Galazo, M.J., Martinez-Cerdeño, V., Porrero, C., and Clascá, F. (2008). Embryonic and postnatal development of the layer I-directed ("matrix") thalamocortical system in the rat. Cereb. Cortex. *18*, 344–363.

Gambino, F., Pagès, S., Kehayas, V., Baptista, D., Tatti, R., Carleton, A., and Holtmaat, A. (2014). Sensory-evoked LTP driven by dendritic plateau potentials in vivo. Nature *515*, 116–119.

Genescu, I., and Garel, S. (2021). Being superficial : a developmental viewpoint on cortical layer 1 wiring. Curr. Opin. Neurobiol. *66*, 125–134.

Gesuita, L., and Karayannis, T. (2021). A 'Marginal' tale: the development of the neocortical layer 1. Curr. Opin. Neurobiol. *66*, 37–47.

Ghezzi, F., Marques-Smith, A., Anastasiades, P.G., Lyngholm, D., Vagnoni, C., Rowett, A., Hoerder-Suabedissen, A., Nakagawa, Y., Molnar, Z., and Butt, S.J.B. (2020). Non-canonical role for Lpar1-EGFP subplate neurons in early postnatal somatosensory cortex. Preprint at BioRxiv. https://doi.org/10.1101/2020.05.12.088450.

Gil-Sanz, C., Franco, S.J., Martinez-Garay, I., Espinosa, A., Harkins-Perry, S., and Müller, U. (2013). Cajal-Retzius cells instruct neuronal migration by coincidence signaling between secreted and contact-dependent guidance cues. Neuron 79, 461–477.

Griveau, A., Borello, U., Causeret, F., Tissir, F., Boggetto, N., Karaz, S., and Pierani, A. (2010). A novel role for Dbx1-derived Cajal-Retzius cells in early regionalization of the cerebral cortical neuroepithelium. PLoS Biol. 8, e1000440.

Hanganu, I.L., Kilb, W., and Luhmann, H.J. (2002). Functional synaptic projections onto subplate neurons in neonatal rat somatosensory cortex. J. Neurosci. 22, 7165–7176.

Harris, K.D., and Shepherd, G.M.G. (2015). The neocortical circuit: themes and variations. Nat. Neurosci. 18, 170–181.

Hartung, J., and Letzkus, J.J. (2021). Inhibitory plasticity in layer 1 – dynamic gatekeeper of neocortical associations. Curr. Opin. Neurobiol. 67, 26–33.

Hoerder-Suabedissen, A., and Molnár, Z. (2013). Molecular diversity of early-born subplate neurons. Cereb. Cortex. 23, 1473–1483.

Huang, Z.J., and Paul, A. (2019). The diversity of GABAergic neurons and neural communication elements. Nat. Rev. Neurosci. 20, 563–572.

Ibrahim, L.A., Mesik, L., Ji, X.Y., Fang, Q., Li, H.-F., Li, Y., Zingg, B., Zhang, L.I., and Tao, H.W. (2016). Cross-modality sharpening of visual cortical processing through layer-1-mediated inhibition and disinhibition. Neuron 89, 1031–1045.

Ibrahim, L.A., Schuman, B., Bandler, R., Rudy, B., and Fishell, G. (2020). ScienceDirect Mining the jewels of the cortex' s crowning mystery. Curr. Opin. Neurobiol. 63, 154–161.

Ibrahim, L.A., Huang, S., Fernandez-Otero, M., Sherer, M., Qiu, Y., Vemuri, S., Xu, Q., Machold, R., Pouchelon, G., Rudy, B., et al. (2021). Bottom-up inputs are required for establishment of top-down connectivity onto cortical layer 1 neurogliaform cells. Neuron 109, 3473–3485.

Iwasato, T., Datwani, A., Wolf, A.M., Nishiyama, H., Taguchi, Y., Tonegawa, S., Knöpfel, T., Erzurumlu, R.S., and Itohara, S. (2000). Cortex-restricted disruption of NMDAR1 impairs neuronal patterns in the barrel cortex. Nature 406, 726–731.

Jabaudon, D., and López Bendito, G. (2012). Development and plasticity of thalamocortical systems. Eur. J. Neurosci. 35, 1522–1523.

Jabaudon, D., Shinder, S.J., Tischfield, D.J., Galazo, M.J., and MacKlis, J.D. (2012). RORβ induces barrel-like neuronal clusters in the developing neocortex. Cereb. Cortex. 22, 996–1006.

Kanold, P.O., and Luhmann, H.J. (2010). The subplate and early cortical circuits. Annu. Rev. Neurosci. 33, 23–48.

Kastli, R., Vighagen, R., van der Bourg, A., Ozgur Argunsah, A., Iqbal, A., Voigt, F.F., Kirschenbaum, D., Aguzzi, A., and Karayannis, T. (2020). Developmental divergence of sensory stimulus representation in cortical interneurons. Preprint at BioRxiv. https://doi.org/10.1101/2020.04.28.065680.

Keller, G.B., and Mrsic-Flogel, T.D. (2018). Predictive processing: a canonical cortical computation. Neuron 100, 424–435.

Kirischuk, S., Luhmann, H.J., and Kilb, W. (2014). Cajal-Retzius cells: update on structural and functional properties of these mystic neurons that bridged the 20th century. Neuroscience 275, 33–46.

Larkum, M.E. (2013). The yin and yang of cortical layer 1. Nat. Neurosci. 16, 114–115.

Ledonne, F., Orduz, D., Mercier, J., Vigier, L., Grove, E.A., Tissir, F., Angulo, M.C., Pierani, A., and Coppola, E. (2016). Targeted inactivation of bax reveals a subtype-specific mechanism of Cajal-Retzius neuron death in the postnatal cerebral cortex. Cell Rep. 17, 3133–3141.

Letzkus, J.J., Wolff, S.B.E., Meyer, E.M.M., Tovote, P., Courtin, J., Herry, C., and Lüthi, A. (2011). A disinhibitory microcircuit for associative fear learning in the auditory cortex. Nature 480, 331–335.

Letzkus, J.J., Wolff, S.B.E., and Lüthi, A. (2015). Disinhibition, a circuit mechanism for associative learning and memory. Neuron 88, 264–276.

Li, H., Fertuzinhos, S., Mohns, E., Hnasko, T.S., Verhage, M., Edwards, R., Sestan, N., and Crair, M.C. (2013). Laminar and columnar development of barrel cortex relies on thalamocortical Neurotransmission. Neuron 79, 970–986.

López-Bendito, G., and Molnár, Z. (2003). Thalamocortical development: how are we going to get there? Nat. Rev. Neurosci. 4, 276–289.

Luhmann, H.J., Sinning, A., Yang, J.W., Reyes-Puerta, V., Stüttgen, M.C., Kirischuk, S., and Kilb, W. (2016). Spontaneous neuronal activity in developing neocortical networks: from single cells to large-scale interactions. Front. Neural Circuits 10, 40.

Luhmann, H.J., Kirischuk, S., and Kilb, W. (2018). The superior function of the subplate in early neocortical development. Front. Neuroanat. 12, 97.

Madisen, L., Zwingman, T.A., Sunkin, S.M., Oh, S.W., Zariwala, H.A., Gu, H., Ng, L.L., Palmiter, R.D., Hawrylycz, M.J., Jones, A.R., et al. (2010). A robust and high-throughput Cre repoting and characterization. Nat. Neurosci. 13, 133–140.

Manita, S., Suzuki, T., Homma, C., Matsumoto, T., Odagawa, M., Yamada, K., Ota, K., Matsubara, C., Inutsuka, A., Sato, M., et al. (2015). A top-down cortical circuit for accurate sensory perception. Neuron 86, 1304–1316.

Manita, S., Miyakawa, H., Kitamura, K., and Murayama, M. (2017). Dendritic spikes in sensory perception. Front. Cell. Neurosci. 11, 29.

De Marco García, Natalia, V., Karayannis, T., and Fishell, G. (2011). Neuronal activity is required for the development of specific cortical interneuron subtypes. Nature 472, 351–355.

De Marco García, N.V., Priya, R., Tuncdemir, S.N., Fishell, G., and Karayannis, T. (2015). Sensory inputs control the integration of neurogliaform interneurons into cortical circuits. Nat. Neurosci. 18, 393–403.

Martini, F.J., Guillamón-Vivancos, T., Moreno-Juan, V., Valdeolmillos, M., and López-Bendito, G. (2021). Spontaneous activity in developing thalamic and cortical sensory networks. Neuron 209, 2519–2534.

Matsui, A., Tran, M., Yoshida, A.C., Kikuchi, S.S., Mami, U., Ogawa, M., and Shimogori, T. (2013). BTBD3 controls DendriteOrientation toward active Axonsin mammalian neocortex. Science 342, 1114–1118.

Meng, X., Yu, Y., Kao, J., and Kanold, P.O. (2020). Transient coupling between subplate and subgranular layers to L1 neurons before and during the critical period. Preprint at BioRxiv. https://doi.org/10.1101/2020.05.05.077784.

Miyoshi, G., Young, A., Petros, T., Karayannis, T., McKenzie Chang, M., Lavado, A., Iwano, T., Nakajima, M., Taniguchi, H., Huang, Z.J., et al. (2015). Prox1 regulates the subtype-specific development of caudal ganglionic eminence-derived GABAergic cortical interneurons. J. Neurosci. 35, 12869–12889.

Mizuno, H., Ikezoe, K., Nakazawa, S., Sato, T., Kitamura, K., and Iwasato, T. (2018). Patchwork-type spontaneous activity in neonatal barrel cortex layer 4 transmitted via thalamocortical projections. Cell Rep. 22, 123–135.

Modol, L., Bollmann, Y., Tressard, T., Baude, A., Che, A., Duan, Z.R.S., Babij, R., De Marco García, N.V., and Cossart, R. (2020). Assemblies of perisomatic GABAergic neurons in the developing barrel cortex. Neuron 105, 93–105.e4.

Molnár, Z., Luhmann, H.J., and Kanold, P.O. (2020). Transient cortical circuits match spontaneous and sensory-driven activity during development. Science 370, eabb2153.

Moreno-Juan, V., Filipchuk, A., Antón-Bolaños, N., Mezzera, C., Gezelius, H., Andrés, B., Rodríguez-Malmierca, L., Susín, R., Schaad, O., Iwasato, T., et al. (2017). Prenatal thalamic waves regulate cortical area size prior to sensory processing. Nat. Commun. 8, 14172.

Myakhar, O., Unichenko, P., and Kirischuk, S. (2011). GABAergic projections from the subplate to Cajal-Retzius cells in the neocortex. Neuroreport 22, 525–529.

Niewoehner, B., Single, F.N., Hvalby, Jensen, V., Meyer Zum Alten Borgloh, S., Seeburg, P.H., Rawlins, J.N.P., Sprengel, R., and Bannerman, D.M. (2007).

Impaired spatial working memory but spared spatial reference memory following functional loss of NMDA receptors in the dentate gyrus. Eur. J. Neurosci. 25, 837–846.

Niquille, M., Limoni, G., Markopoulos, F., Cadilhac, C., Prados, J., Holtmaat, A., and Dayer, A. (2018). Neurogliaform cortical interneurons derive from cells in the preoptic area. Elife 7, e32017.

Ohtaka-Maruyama, C. (2020). Subplate neurons as an organizer of mammalian neocortical development. Front. Neuroanat. 14, 8.

Palmer, L.M., Clark, B.A., Gründemann, J., Roth, A., Stuart, G.J., and Häusser, M. (2010). Initiation of simple and complex spikes in cerebellar Purkinje cells. J. Physiol. 588, 1709–1717.

Palmer, L.M., Shai, A.S., Reeve, J.E., Anderson, H.L., Paulsen, O., and Larkum, M.E. (2014). NMDA spikes enhance action potential generation during sensory input. Nat. Neurosci. 17, 383–390.

Pnevmatikakis, E.A., and Giovannucci, A. (2017). NoRMCorre: an online algorithm for piecewise rigid motion correction of calcium imaging data. J. Neurosci. Methods 291, 83–94.

Pnevmatikakis, E.A., Soudry, D., Gao, Y., Machado, T.A., Merel, J., Pfau, D., Reardon, T., Mu, Y., Lacefield, C., Yang, W., et al. (2016). Simultaneous denoising, deconvolution, and demixing of calcium imaging data. Neuron 89, 285.

Poorthuis, R.B., Muhammad, K., Wang, M., Verhoog, M.B., Junek, S., Wrana, A., Mansvelder, H.D., and Letzkus, J.J. (2018). Rapid Neuromodulation of layer 1 interneurons in human neocortex. Cell Rep. 23, 951–958.

Rhoades, R.W., Bennett-Clarke, C.A., Chiaia, N.L., White, F.A., Macdonald, G.J., Haring, J.H., and Jacquin, M.F. (1990). Development and lesion induced reorganization of the cortical representation of the rat's body surface as revealed by immunocytochemistry for serotonin. J. Comp. Neurol. 293, 190–207.

Riva, M., Genescu, I., Habermacher, C., Orduz, D., Ledonne, F., Rijli, F.M.F.M., López-Bendito, G., Coppola, E., Garel, S., Angulo, M.C.M.C., et al. (2019). Activity-dependent death of transient cajal-retzius neurons is required for functional cortical wiring. Elife 8, e50503.

Rogan, S.C., and Roth, B.L. (2011). Remote control of neuronal signaling. Pharmacol. Rev. 63, 291–315.

Rubio-garrido, P., Pérez-De-Manzo, F., Porrero, C., Galazo, M.J., Clascá, F., Pe, F., Galazo, M.J., and Clasca, F. (2009). Thalamic input to distal apical dendrites in neocortical layer 1 is massive and highly convergent. Cereb. Cortex. 19, 2380–2395.

Ruiz-Reig, N., Andrés, B., Huilgol, D., Grove, E.A., Tissir, F., Tole, S., Theil, T., Herrera, E., and Fairén, A. (2017). Lateral thalamic eminence: a novel origin for mGluR1/lot cells. Cereb. Cortex. 27, 2841–2856.

Schuman, B., Machold, R.P., Hashikawa, Y., Fuzik, J., Fishell, G.J., and Rudy, B. (2018). Four unique interneuron populations reside in neocortical layer 1. J. Neurosci. 39, 125–139.

Schuman, B., Dellal, S., Prönneke, A., MacHold, R., and Rudy, B. (2021). Neocortical layer 1: an elegant solution to top-down and bottom-up integration. Annu. Rev. Neurosci. 44, 221–252.

Shin, B.J.N., Doron, G., and Larkum, M.E. (2021). Memories off the top of your head. Science 374, 538–540.

Sur, M., and Rubenstein, J.L.R. (2005). Patterning and plasticity of the cerebral cortex. Science 310, 769–773.

Suzuki, M., and Larkum, M.E. (2020). General anesthesia decouples cortical pyramidal neurons. Cell 180, 666–676.e13.

Takahashi, N., Oertner, T.G., Hegemann, P., and Larkum, M.E. (2016). Active cortical dendrites modulate perception. Science 354, 1159–1165.

Takahashi, N., Ebner, C., Sigl-Glöckner, J., Moberg, S., Nierwetberg, S., and Larkum, M.E. (2020). Active dendritic currents gate descending cortical outputs in perception. Nat. Neurosci. 23, 1277–1285.

Tissir, F., Ravni, A., Achouri, Y., Riethmacher, D., Meyer, G., and Goffinet, A.M. (2009). DeltaNp73 regulates neuronal survival in vivo. Proc. Natl. Acad. Sci. U S A 106, 16871–16876.

Tremblay, R., Lee, S., and Rudy, B. (2016). GABAergic interneurons in the neocortex: from cellular properties to circuits. Neuron 91, 260–292.

Tsien, J.Z., Huerta, P.T., and Tonegawa, S. (1996). The Essential Role of Hippocampal CA1 NMDA Receptor-Dependent Synaptic Plasticity in Spatial Memory. Cell 87, 1327–1338.

Tuncdemir, S.N., Wamsley, B., Stam, F.J., Callaway, E.M., Rudy, B., Fishell, G., Tuncdemir, S.N., Wamsley, B., Stam, F.J., Osakada, F., et al. (2015). Early somatostatin interneuron connectivity mediates the maturation of deep layer cortical circuits. Neuron 89, 521–535.

Villar-Cerviño, V., Molano-Mazón, M., Catchpole, T., Valdeolmillos, M., Henkemeyer, M., Martínez, L.M., Borrell, V., and Marín, O. (2013). Contact repulsion controls the dispersion and final distribution of Cajal-Retzius cells. Neuron 77, 457–471.

Williams, L.E., and Holtmaat, A. (2019). Higher-order thalamocortical inputs gate synaptic long-term potentiation via disinhibition. Neuron 101, 91–102.

Yoshida, M., Assimacopoulos, S., Jones, K.R., and Grove, E.A. (2006). Massive loss of Cajal-Retzius cells does not disrupt neocortical layer order. Development 133, 537–545.

Zhu, H., Aryal, D.K., Olsen, R.H.J., Urban, D.J., Swearingen, A., Forbes, S., Roth, B.L., and Hochgeschwender, U. (2016). Cre-dependent DREADD (Designer Receptors Exclusively Activated by Designer Drugs) mice. Genesis 54, 439–446.

Zhuang, X., Masson, J., Gingrich, J.A., Rayport, S., and Hen, R. (2005). Targeted gene expression in dopamine and serotonin neurons of the mouse brain. J. Neurosci. Methods 143, 27–32.

STAR★METHODS

KEY RESOURCES TABLE

REAGENT or RESOURCE	SOURCE	IDENTIFIER
Antibodies		
Rabbit anti-DsRed	Takara	RRID: AB_10013483
Rabbit anti-Prox1	Abcam	RRID: AB_2170708
Goat anti-Prox1	R&D	RRID: AB_2170716
Rabbit anti-NPY	ImmunoStar	RRID: AB_2307354
Mouse anti-Reelin	Merck Millipore	RRID: AB_2179313
Rabbit anti-Calretinin	Swant	RRID: AB_2721226
Rabbit anti-Cux1	Santa-Cruz	RRID: AB_2261231
Rat anti-Somatostatin	Merk Milipore	RRID: AB_2255365
Rabbit anti-Parvalbumin	Swant	RRID: AB_2631173
Chicken anti-GFP	Aves	RRID: AB_10000240
Mouse anti-NeuN	Merk Millipore	RRID: AB_2298772
Guinea Pig anti-VGlut2	Merk Millipore	RRID: AB_2665454
Alexa Fluor 488 conjugated donkey anti-mouse IgG	Jackson ImmunoResearch Laboratories	RRID: AB_2572300
Cy3-AffiniPure Donkey anti-mouse IgG	Jackson ImmunoResearch Laboratories	RRID: AB_2340813
Alexa Fluor 488 conjugated donkey anti-rabbit	Jackson ImmunoResearch Laboratories	RRID: AB_2492289
Cy3-AffiniPure Donkey anti-rabbit	Jackson ImmunoResearch Laboratories	RRID: AB_2307443
Cy5-AffiniPure Donkey anti-rabbit	Jackson ImmunoResearch Laboratories	RRID: AB_2340607
Alexa Fluor 488 conjugated donkey anti-chicken	Jackson ImmunoResearch Laboratories	RRID: AB_2340375
Alexa Fluor 488 conjugated donkey anti-guinea pig	Jackson ImmunoResearch Laboratories	RRID: AB_2340472
Cy5-AffiniPure Donkey anti-goat	Jackson ImmunoResearch Laboratories	RRID: AB_2340415
Cy3-AffiniPure Donkey anti-rat	Jackson ImmunoResearch Laboratories	RRID: AB_2340666
Chemicals, virus, peptides and recombinant proteins		
Hoechst	Sigma-Aldrich	Cat#: 33342
Paraformaldehyde	Sigma-Aldrich	Cat#: P6148
Tamoxifen	Sigma-Aldrich	Cat#: T5648
Corn oil	Sigma-Aldrich	Cat#: C8267
Triton 100X	Eurobio	Cat#: GAUTTR00-07
AAV1.CaMKII.GCaMP6f.WPRE.SV40	Addgene	Cat#: Addgene_100834
Experimental models: Organisms/strains		
ΔNp73creIRESGFP	Tissir et al., 2009	provided by Tissir Laboratory
Tg(Thy1-YFP)HJrs	Feng et al., 2000; The Jackson Laboratory	*B6.Cg-Tg(Thy1-YFP)HJrs/J*
ROSA26^loxP-stop-loxP-Tomato	Madisen et al., 2010; The Jackson Laboratory	*B6.Cg-Gt(ROSA)26Sortm9 (CAG-tdTomato)Hze/J*
ROSA26^Kir2.1mCherry/+	Moreno-Juan et al., 2017	provided by López-Bendito Laboratory
Gbx2^creERT2/+	Chen et al., 2009, The Jackson Laboratory	*Gbx2tm1.1(cre/ERT2)Jyhl/J*
Sert^cre/+	Zhuang et al., 2005, The Jackson Laboratory	*B6.129(Cg)-Slc6a4^tm1(cre)Xz/J*
GluN1^flox	Tsien et al., 1996, The Jackson Laboratory	*B6.129S4-Grin1^tm2Stl/J*

Continued

REAGENT or RESOURCE	SOURCE	IDENTIFIER
ROSA26^hM3Dq-DREADD/+	Zhu et al., 2016, The Jackson Laboratory	B6N;129-Tg(CAG-CHRM3*,-mCitrine)1Ute/J
ROSA26^flox-stop-flox-dt-a	Brockschnieder et al., 2006	B6;129-Gt(ROSA)26Sortm1(DTA)Mrc/J
Software and algorithms		
GraphPad Prism 7.0	GraphPad Software	RRID: SCR_000306
ImageJ/FIJI	NIH	RRID: SCR_002285
Adobe Photoshop CS6	Adobe Systems	RRID: SCR_014199
Adobe Illustrator CS6	Adobe Systems	RRID: SCR_010279
MESc FEMTOSmart software	Femtonics	N/A
MATLAB	MathWorks	RRID: SCR_001622

RESOURCE AVAILABILITY

Lead contact
Further requests and information concerning this study, should be addressed to the lead contact, Sonia Garel (garel@biologie.ens.fr).

Materials availability
This study did not generate new reagents.

Data and code availability
- All the raw data generated in this study is freely available upon request, to the lead contact, Sonia Garel (garel@biologie.ens.fr).
- This paper does not contain original code.
- Any additional information required to reanalyze the data reported in this paper is available from the lead contact upon request.

EXPERIMENTAL MODEL AND SUBJECT DETAILS

Animals
ΔNp73^creIRESGFP (*ΔNp73*^cre) (Tissir et al., 2009), *R26*^loxP-stop-loxPtdTomato (*R26*^mT/mT) (Madisen et al., 2010), *GluN1*^flox/flox (Niewoehner et al., 2007), *Thy1::YFP* (Feng et al., 2000), *R26*^flox-stop-flox-dt-a/+ (*R26*^dt-a/+) (Brockschnieder et al., 2006) and *R26*^hM3Dq-DREADD (*R26*^DR/DR) (JAX026220 B6N; 129-Tg(CAG-CHRM3*,-mCitrine)1Ute/J) mice were kept in a C57BL/6J background, while *R26*^Kir2.1-mCherry/+ (*R26*^Kir2.1/+) (Moreno-Juan et al., 2017), *Gbx2*^creERT2/+ (Chen et al., 2009) and *Sert*^cre/+ (B6.129(Cg)-Slc6a4^tm1(cre)Xz/J, Zhuang et al., 2005) mice were kept in a ICR/CD-1 background. All animals were housed in a 12 h light-dark cycle and both males and females were used in this study. *ΔNp73*^cre mice were crossed with the *R26*^loxP-stop-loxPtdTomato (*R26*^mT/mT) reporter line (Madisen et al., 2010) to permanently label CRc subtypes, with the *R26*^flox-stop-flox-dt-a/+ (*R26*^dt-a/+) line (Brockschnieder et al., 2006) to induce the partial elimination of CRc, with the *GluN1*^flox/flox (*GluN1*^fl/fl) line (Niewoehner et al., 2007) to inactivate GluN1 function specifically in CRc, with the *R26*^Kir2.1/+ line to overexpress the Kir2.1 channel in CRc, with the *R26*^DR/DR to express the receptor hM3Dq-DREADD receptor specifically in CRc, which upon CNO injection drives overactivation. *Sert*^cre/+ and *Gbx2*^creERT2/+ mice were crossed with the *R26*^Kir2.1/+ line to enable the hyperpolarization of sensory thalamic nuclei or of most thalamic nuclei respectively (Antón-Bolaños et al., 2019; Moreno-Juan et al., 2017). *Thy1::YFP* mice were crossed with the *R26*^-dt-a line to generate in *R26*^-dt-a;*Thy1::YFP* animals that were subsequently backcrossed with *ΔNp73*^cre line to enable the visualization of L5 pyramidal neurons in models with decreased CRc density. *Thy1::YFP* mice were crossed with *R26*^DR/DR mice to generate *R26*^DR/+;*Thy1::YFP* animals. The latter mice were crossed with *ΔNp73*^cre animals to enable a modulation of CRc density and a visualization of L5 pyramidal neurons. Littermates not expressing the *cre* were used as controls for each cross. Animals were genotyped by PCR using primers specific for the different alleles as defined by the provider or initial publications. The day of the vaginal plug was considered E0.5 and the birth date was considered as postnatal day 0 (P0). Animals were handled in accordance with European regulations and the local ethics committee.

METHODS DETAILS

Drug administration
Tamoxifen induction of Cre-ERT2 recombination in the *Gbx2*^creERT2/+ was performed by gavage administration of tamoxifen (5 mg dissolved in corn oil, Sigma) at E10.5 to target all sensory thalamic nuclei, as previously described (Antón-Bolaños et al., 2019). The excitatory DREADD receptor in *R26*^DR/DR (*R26*^hM3Dq-DREADD) mice was activated through injections of its exogenous ligand Clozapine N-oxide (CNO) (Rogan and Roth, 2011). CNO (Tocris 4936) was diluted with 0.9% saline to 0.5 mg/mL. Pups were injected with vehicle (0.9% saline) or CNO (5 mg/kg) subcutaneously, twice a day, from P1 to P3.

Sensory deprivation

Whisker plucking of pups was performed bilaterally from P1 to P3 as previously described (De Marco García et al., 2015). Pups were removed from the mother, anesthetized by hypothermia for 3 min and whiskers were plucked with sterile forceps. The Infraorbital Nerve (ION) lesion was performed unilaterally at P1, as previously described (Frangeul et al., 2014; Rhoades et al., 1990). In brief, pups were removed from the mother and anesthetized by hypothermia for 3 min. Using a sterile scalpel, an incision was made between the eye and the right whisker pad, enabling the section of the ION. Pups were put on a heating pad to recover from the lesion and anesthesia. The efficiency of the manipulation was systematically checked by anti-vGlut2 immunostaining to assess for the absence of barrels in the contralateral somatosensory cortex.

Viral injection

The mice were anesthetized using isoflurane. Adequate anesthesia was assessed (absence of toe pinch reflexes, corneal reflexes, and vibrissae movement). Dehydration was prevented by injecting sterile saline by subcutaneous (s.c) injection. A ~3*3 mm craniotomy was then made using a pneumatic dental drill. Stereotaxic injections were then targeted to the layer 5 and 200 nL of virus (AAV1.CaMKII.GCaMP6f.WPRE.SV40) were injected at a maximum rate of 60 nL/min, using a glass pipette (Wiretrol, Drummond) attached to an oil hydraulic manipulator (MO-10, Narishige). After injections, the virus was allowed to diffuse for at least 20 min before the pipette was withdrawn. The craniotomy was covered with sterile saline and sealed with a 3 mm glass coverslip. The coverslip was sealed to the skull using dental acrylic and dental cement (Jet Repair Acrylic, Lang Dental Manufacturing). Mice were then waked-up by a subcutaneous injection of a mixture containing atipamezole (2.5 mg/kg), flumazenil (0.5 mg/kg) and buprenorphine (0.1 mg/kg). A delay of 2–3 weeks for recovery was respected before imaging, during which the body weight of mice was daily checked.

Two-photon calcium imaging of dendritic activity and analysis
Anesthesia

Anesthesia was induced using isoflurane (4% containing ~0.5 L min^{-1} O2) and then continued using an intraperitoneal (i.p.) injection of a mixture (MMB) (5 μL/g) composed of medetomidine (0.2 mg/kg), midazolam (0.2 mg/kg), and buprenorphine (0.2 mg/kg). A heating-pad was positioned underneath the animal to keep the body temperature at 37°C. Eye dehydration was prevented by topical application of ophthalmic gel. Analgesia was achieved by local application of 100 μL of lidocaine (lurocaine, 1%) and s.c. injection of buprenorphine (0.05 mg/kg). To prevent risks of inflammation and brain swelling 40 μL of dexamethasone (0.1 mg/mL) were injected intramuscularly (i.m.) before the surgery. After disinfection of the skin (with modified ethanol 70% and betadine), the skull was exposed and a ~5 mm plastic chamber was attached to it above the relative stereotaxic location of the C2 barrel column (−1.5 mm from bregma, + 3.3 mm midline) using a combination of super glue (Loctite) and dental cement (Jet Repair Acrylic, Lang Dental Manufacturing). The chamber was filled with saline (0.9% NaCl) and sealed with a glass coverslip.

Intrinsic optical imaging for barrel column targeting

To locate the cortical barrel column corresponding to the whisker C2, intrinsic optical signals (IOS) were imaged as previously described (Campelo et al., 2020), through the intact skull using a light guide system with a 700 nm (bandwidth of 20 nm) interference filter and stable 100-W halogen light source. Briefly, the head of the animal was stabilized using a small stereotaxic frame and the body temperature kept constant with a heating pad. An image of the surface vascular pattern was taken using a green light (546 nm-interference filter) at the end of each imaging session. Images were acquired using the Imager 3001F (Optical Imaging, Mountainside, NJ) equipped with a large spatial 256 × 256 array, fast readout, and low read noise charge-coupled device (CCD) camera. The size of the imaged area was adjusted by using a combination of two lenses with different focal distances (upper lens: Nikon 135 mm, f2.0; bottom lens: Nikon 50 mm, f1.2). The CCD camera was focused on a plane 300 μm below the skull surface. Images were recorded at 10 Hz for 5 sec., with a spatial resolution of 2.75 μm/pixel comprising a total area of 2.7 × 2.7 mm^2. The whisker C2 was deflected back and forth (8 Hz, 2.5 sec.) using a glass-capillary attached to a piezoelectric actuator (PL-140.11 bender controlled by an E−650 driver; Physik Instrumente) triggered by a pulse stimulator (Master-8, A.M.P.I.). Each trial consisted of a 1 sec. baseline period (frames 1–10), followed by a response period (frames 11–22) and a post-stimulus period (frames 23–50). Intertrial intervals lasted 20 sec. to avoid contamination of the current IOS by prior stimulations. IOS were computed by subtracting each individual frame of the response period by the average baseline signal. The obtained IOS was overlapped with the vasculature image using ImageJ software to precisely identify the cortical region corresponding to the whisker C2.

In vivo calcium imaging

Two weeks after surgery, a custom-made stainless-steel head stage was attached to the skull using dental acrylic and dental cement. Animals were anaesthetized for imaging using isoflurane (1% with 0.5 L/min O$_2$). Spontaneous vibrissae movements were controlled using an infra-red camera and avoided using supplementary isoflurane if necessary. Fluorescence was acquired with an *in vivo* non-descanned FemtoSmart two-photon laser-scanning microscope (2PLSM, Femtonics) equipped with a x16 objective (0.8 NA, Nikon). The microscope, acquisition parameters and the TTL-driven synchronization between acquisition and whisker stimulation were controlled by the MES software (Femtonics). The GCaMP were excited using a Ti:sapphire laser operating at λ = 910 nm (Mai Tai DeepSee, Spectra-Physics) with an average excitation power at the focal point lower than 50 mW. Fluorescence change was measured in these Ca^{2+} sources as follows. Time-series of fluorescence levels corresponding to these dendritic domains were obtained by pixel-based averaging over the masks of the dendritic spines in the registered, non-denoised, image stacks.

For each animal, time-series images were acquired within a field-of-view of 90 × 90 μm corresponding to the cortical region with maximum IOS. The whisker C2 was preferentially deflected with brief air puffs synchronized with imaging acquisition using a TTL.

Tissue preparation and immunohistochemistry

Animals were anesthetized with Isoflurane and intracardially perfused with 4% paraformaldehyde (PFA) in 0.1 M PBS, pH 7.4 and post-fixed over-night in 4% PFA at 4°C. Brains were embedded in 3.5% agarose and sectioned into 70 μm free-floating slices at all stages for all genetic models except for crosses including the *Thy1::YFP* allele that were cut into and 300 μm free-floating sections to visualize whole dendritic arbors. Immunostaining was performed as previously described (de Frutos et al., 2016). Primary antibodies used for immunohistochemistry were: mouse anti-Reelin (MAB5364, Millipore, 1:300), rabbit anti-DsRed (632,496, Takara, 1:500), goat anti-Prox1(AF2727, R&D Systems, 1:500), rabbit anti-Prox1 (ab38692, Abcam, 1:300), rabbit anti-NPY (22940, Immunostar, 1:1000), rat anti-SST (MAB354, Millipore, 1:50), chicken anti-gfp (Gfp-1020, Aves, 1:1000), guinea pig anti-vGlut2 (AB2251-I, Millipore, 1:1000), rabbit anti-Cux1 (AB-2261231, Santa-Cruz Biotechnology, 1:300), rabbit anti-Calretinin (7697, Swant, 1:1000), rabbit anti-Parvalbumin (PV27, Swant, 1:1000), mouse anti-NeuN (MAB377, Millipore, 1:300). Secondary antibodies used against primary antibodies were: donkey anti-mouse Alexa-488 (Jackson ImmunoResearch Laboratories, 1:800), donkey anti-mouse Cy3 (Jackson ImmunoResearch Laboratories, 1:800), donkey anti-chicken Alexa-488 (Jackson ImmunoResearch Laboratories, 1:800), donkey anti-guinea pig Alexa-488 (Jackson ImmunoResearch Laboratories, 1:800), donkey anti-rabbit Alexa-488 (Jackson ImmunoResearch Laboratories, 1:800), donkey anti-rabbit Cy3 (Jackson ImmunoResearch Laboratories, 1:800), donkey anti-rabbit Cy5 (Jackson ImmunoResearch Laboratories, 1:800), donkey anti-goat Cy5 (Jackson ImmunoResearch Laboratories, 1:800), donkey anti-rat Cy3 (Jackson ImmunoResearch Laboratories, 1:800). Hoechst (Sigma-Aldrich 33342, 1:1000) was used for fluorescent nuclear counterstaining and Vectashield for mounting (Vector Labs).

QUANTIFICATIONS AND STATISTICAL ANALYSIS

Image acquisition and quantification

Immunofluorescence images were acquired using a confocal microscope (Leica TCS SP5) with objectives of either 10X, 25X, 40X and 63X, with or without optical zoom. Cellular and spine quantifications were performed using the ImageJ software, in the somatosensory barrel cortex or Lateral Olfactory tract (LOT) for the respective ages and genotypes. For each section, the density of CRc was calculated as number of CRc/1 mm length of L1 on a 10μm-thick optical section, measured using ImageJ software. Hoechst staining was used to discriminate different cortical layers for cellular quantifications per layer of the neocortex. The area used for quantifications of CRc in the LOT was also defined using Hoechst staining (86748.4 μm^2 at P7 and 452741.04 μm^2 at P25).

Analysis of calcium imaging

Dendrites were automatically identified and their Ca^{2+} transient activity extracted thanks to a customized analysis pipeline. First, images were stabilized to cope for lateral motion of the field-of-view using an elastic registration method (Pnevmatikakis and Giovannucci, 2017). GCaMP fluorescence, in the green channel, proved unreliable to compute deformations because of the transient nature of the Ca^{2+} signals. Instead, we used the more-stable autofluorescence images (red-shifted channel) to compute local deformations and then locally corrected GCaMP images according to these displacements. Out-of-focus images, caused by movements of the brain along the optical axis, where then discarded by analyzing fluctuations of the autofluorescence images: images for which the mean autofluorescence changed by more than 10% from the baseline level were discarded. Then we used a de-noising custom method to improve the signal-to-noise ratio of selected images. It consists in removing pixel-wise noise, while preserving the local pixel-to-pixel covariance by using a localized principal component analysis and applying a threshold to transformed coefficients. Dendritic domains with asynchronous Ca^{2+} activity were then automatically identified by using a custom source separation method based on the non-negative matrix factorization method, akin to (Pnevmatikakis et al., 2016). Time-series of fluorescence levels corresponding to these dendritic domains were obtained by pixel-based averaging over the masks of the dendritic spines in the registered, non-denoised, image stacks.

STATISTICAL ANALYSIS

All data were expressed as mean ± SEM. A P-value less than 0.05 was considered significant. According to the data structure, we systematically performed non-parametric tests namely Mann-Whitney U Test, Kruskal-Wallis Tests with Dunn's correction, and 2 ways ANOVA test with Dunnett's or Sidak's correction, depending on whether we performed single or multiple group comparisons with individual or common controls. Statistics and plotting were performed using GraphPad Prism 7.00 (GraphPad Software Inc., USA). $*p < 0.05$, $**p < 0.01$, $***p < 0.001$.

Supplemental information

Dynamic interplay between thalamic

activity and Cajal-Retzius cells

regulates the wiring of cortical layer 1

Ioana Genescu, Mar Aníbal-Martínez, Vladimir Kouskoff, Nicolas Chenouard, Caroline Mailhes-Hamon, Hugues Cartonnet, Ludmilla Lokmane, Filippo M. Rijli, Guillermina López-Bendito, Frédéric Gambino, and Sonia Garel
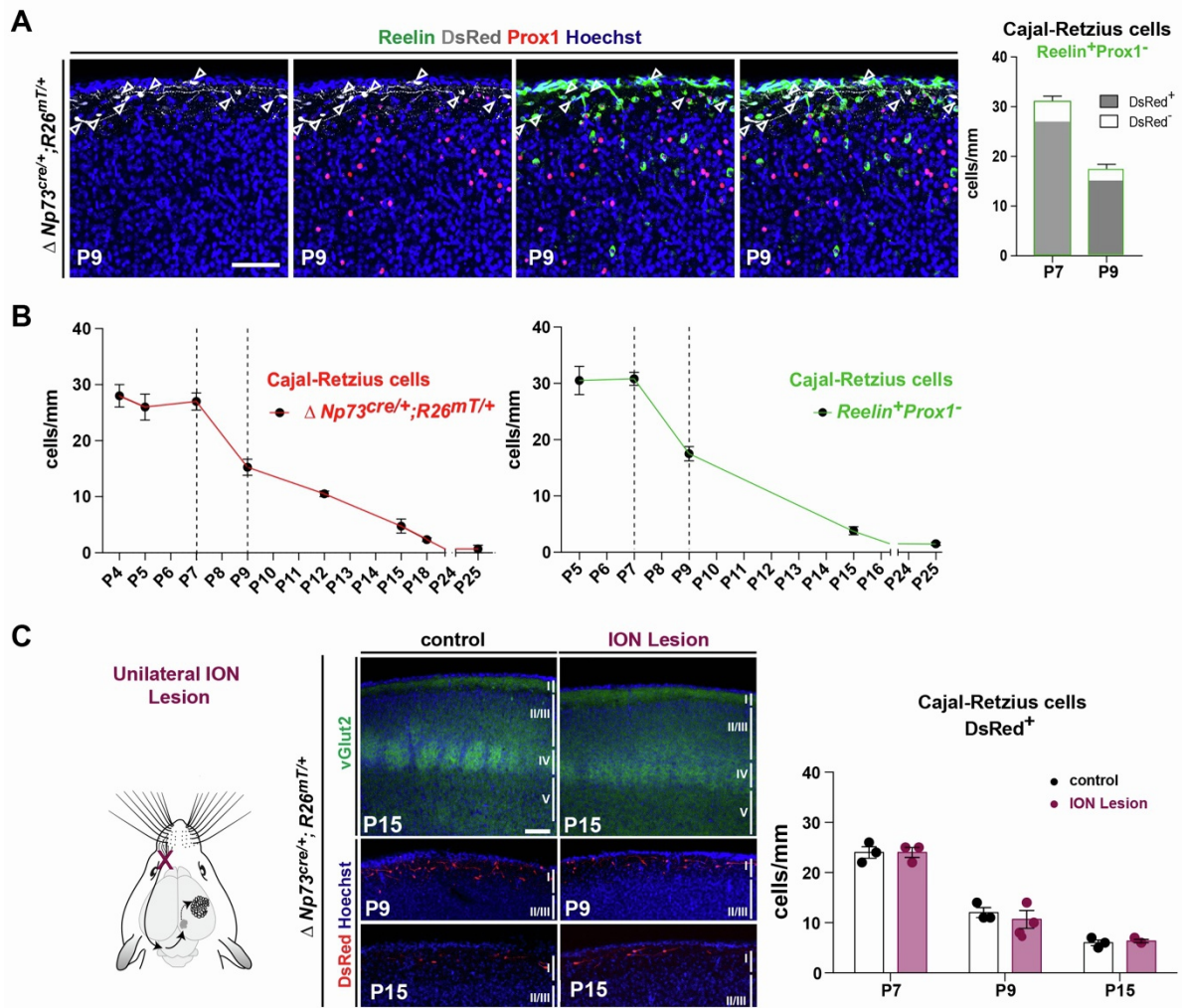
Figure S1, related to Figure 1. Different labelling strategies highlight Cajal-Retzius cell dynamics across development and sensory deprivation.

(A) Identification of Cajal-Retzius cells using the $\Delta Np73^{cre/+};R26^{mT/+}$ driver and co-immunostaining as Reelin$^+$Prox1$^-$ cells at P9. Quantifications of the percentage of the $\Delta Np73^{cre/+};R26^{mT/+}$CRc out of the total number of CRc labelled with Reelin$^+$Prox1$^-$ (right). At P7, 86.96% of the Reelin$^+$Prox1$^-$ are DsRed$^+$ in the $\Delta Np73^{cre/+};R26^{mT/+}$ line and at P9, 87.14% of the Reelin$^+$Prox1$^-$ are DsRed$^+$ in the $\Delta Np73^{cre/+};R26^{mT/+}$ line, consistently with previous reports (Ledonne et al., 2016; Tissir et al., 2009) showing that the $\Delta Np73^{cre/+}$line targets approximatively 85% of CRc, as it does not label pallial-subpallial boundary-derived CRc (P7: n=22 for Reelin$^+$Prox1$^-$ and n=6 for DsRed$^+$; P9: n=18 for Reelin$^+$Prox1$^-$ and n=4 for DsRed$^+$). **(B)** Density of CRc (cells/mm length of L1) evaluated by genetic labeling ($\Delta Np73^{cre/+}$) and by co-immunostaining (Reelin$^+$Prox1$^-$) at early postnatal stages reveal an acute period of elimination between P7 and P9 until their almost complete elimination in the somatosensory cortex by P25. **(C)** Schematic representation of a unilateral InfraOrbital Nerve (ION) lesion (left). Confocal images of sections across the barrel cortex (S1bf) of $\Delta Np73^{cre/+};R26^{mT/+}$ at P7, P9 and P15 in control and ION lesioned pups immunostained for DsRed (red) to label CRc. At P15, vGlut2 immunostaining reveals the lack of visible barrels in ION lesioned pups (middle). Quantification of CRc density (cells/mm of L1 length) shows no differences in controls and ION-lesioned pups (P7: n=3 controls, n=3 ION; P9: n=3 controls and n=3 ION, P15: n=3 controls and n=3 ION) (right). Values are expressed as mean ± SEM, 2-ways ANOVA test with Sidak's multiple comparison correction, *p < 0.05, **p< 0.01, ***p < 0.001. Scale bar represents 100µm.

1
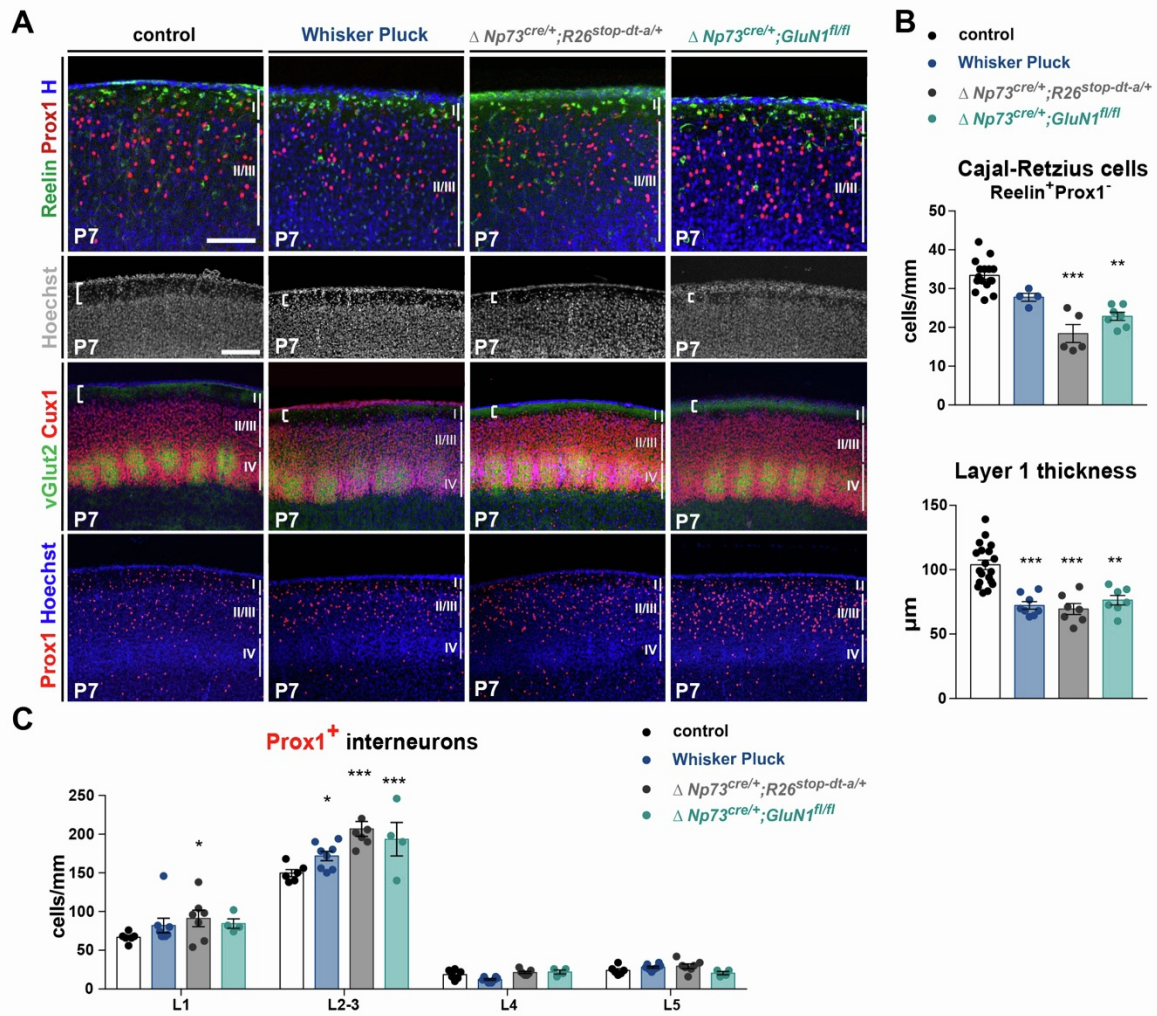
Figure S2, related to Figure 2. Sensory deprivation and decrease in Cajal-Retzius cell density alter L1 thickness and interneuron distribution in the first postnatal week.
(A) Confocal images of coronal sections in the barrel cortex (S1bf) of P7 controls, animals that were Whisker Plucked postnatally (WP), $\Delta Np73^{cre/+};R26^{dt-a/+}$ and $\Delta Np73^{cre/+};GluN1^{fl/fl}$ mutants. White brackets delineate L1. (B) Quantification of CRc numbers (in cells/mm of L1 length) identified as Reelin$^+$Prox1$^-$ cells at P7 (n=16 for controls, n=4 for WP, n=5 for $\Delta Np73^{cre/+};R26^{dt-a/+}$ and n=7 for $\Delta Np73^{cre/+};GluN1^{fl/fl}$ mutants) and of L1 thickness (in μm) (n=19 for control, n=8 for WP, n=7 for $\Delta Np73^{cre/+};R26^{dt-a/+}$ mutants and n=7 for $\Delta Np73^{cre/+};GluN1^{fl/fl}$ mutants). (C) Quantification of Prox1$^+$ interneuron distribution in each layer of the neocortex reveals an increase in all experimental conditions, compared to controls (n=5 for controls, n=8 for WP condition, n=7 for $\Delta Np73^{cre/+};R26^{dt-a/+}$ and n=4 for $\Delta Np73^{cre/+};GluN1^{fl/fl}$ mutants). Values are expressed as mean ± SEM, Kruskal-Wallis multiple comparison test in (B) and 2-ways ANOVA with Dunnett's multiple comparison correction in (C). * p<0.05; **p<0.001; ***p<0.0001. Scale bar represents 200 μm.
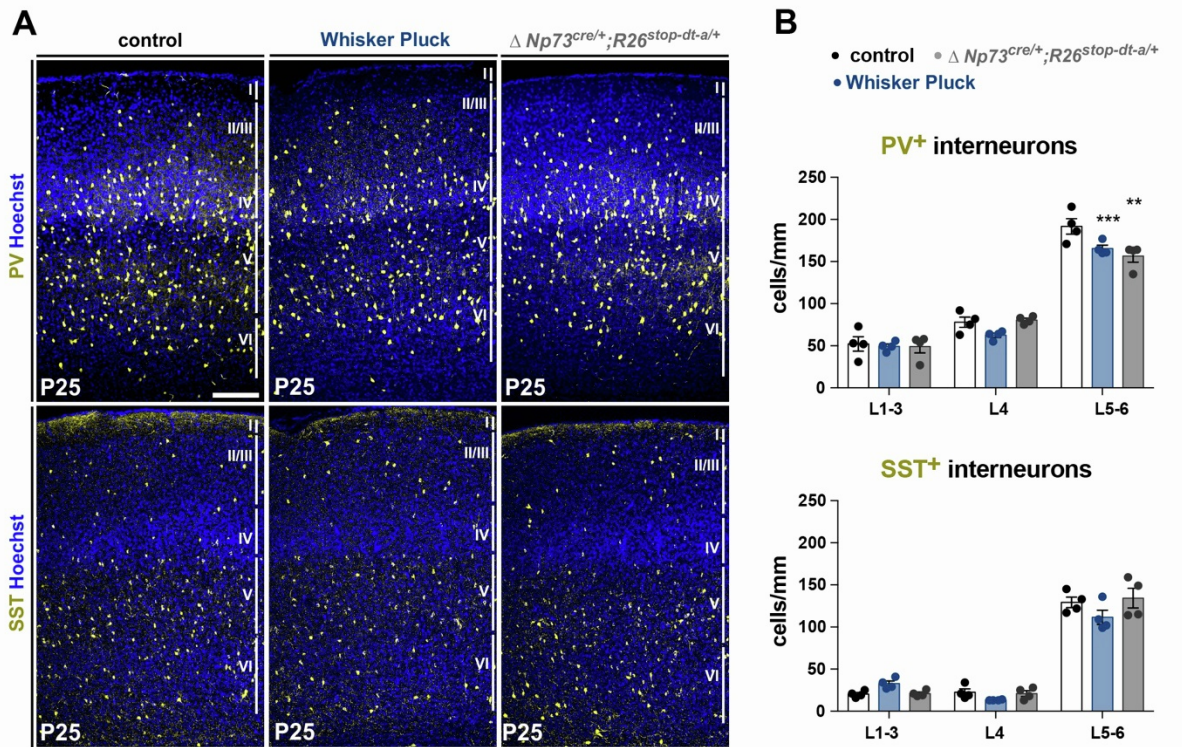
Figure S3, related to Figure 3. Sensory deprivation and a decrease in Cajal-Retzius cell density modify PV⁺ interneuron distribution.

(A) Confocal images of coronal sections in the barrel cortex (S1bf) of P25 controls, animals that were Whisker Plucked postnatally (WP) and *ΔNp73^{cre/+};R26^{dt-a/+}* mutants showing PV and SST immunostainings, that mark two non-overlapping populations of MGE-derived interneurons. (B) Quantifications of MGE-derived interneuron density in upper cortical layers (L1-3), layer 4 and deep cortical layers (L5-6), showing a selective impact on the distribution of PV⁺ interneurons in both experimental models (n=4 for controls, n=4 for WP and n=4 for *ΔNp73^{cre/+};R26^{dt-a/+}* mutants). Values are expressed as mean ± SEM, 2-ways ANOVA with Dunnett's multiple comparison correction, * $p<0.05$; **$p<0.001$; ***$p<0.0001$. Scale bar represents 200 µm.
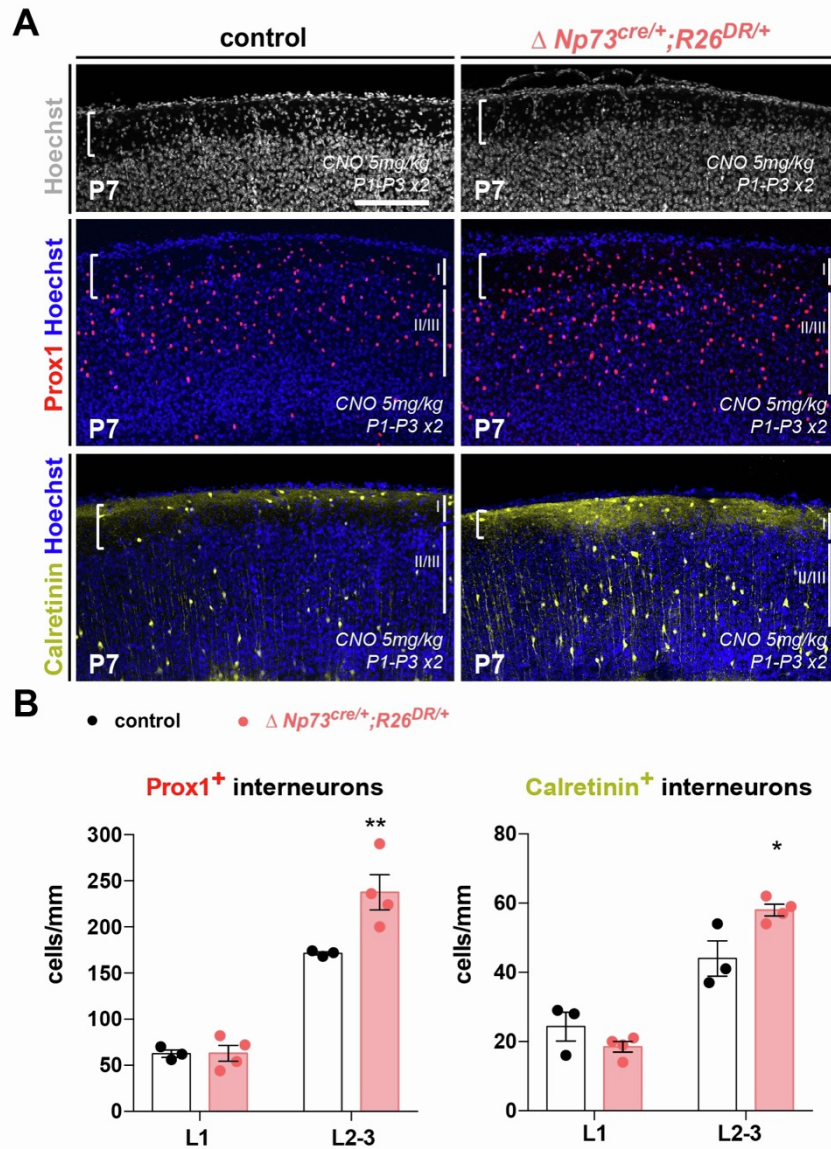
Figure S4, related to Figure 5. Reduction in both prenatal and postnatal CRc density perturb interneuron distribution at P7.
(A) Confocal images of coronal sections in the barrel cortex of P7 controls and $\Delta Np73^{cre/+};R26^{DR/+}$ mutants, both having received CNO injections between P1 and P3. Immunostainings against Prox1 that labels all POA/CGE-derived interneurons and against Calretinin which labels a subpopulation called bipolar neurons. **(B)** Quantifications of Prox1$^+$ and Calretinin$^+$ interneuron densities in L1 and L2-3 in the barrel cortex of P7 controls and $\Delta Np73^{cre/+};R26^{DR/+}$ mutants, showing an increase in interneuron numbers in both mutant backgrounds (Prox1: n=3 for controls and n=4 for $\Delta Np73^{cre/+};R26^{DR/+}$ mutants; Calretinin: n=3 for controls and n=4 for $\Delta Np73^{cre/+};R26^{DR/+}$ mutants). Values are expressed as mean ± SEM, 2-ways ANOVA with Sidak's multiple comparison correction in (B), * $p<0.05$; **$p<0.001$; ***$p<0.0001$. Scale bar represents 200 μm.